Structure-property relationships in actinide containing molten salts – A review
Understanding and modelling the chemistry of nuclear fuel salts

Smith, A. L.

DOI
10.1016/j.molliq.2022.119426

Publication date
2022

Document Version
Final published version

Published in
Journal of Molecular Liquids

Journal of Molecular Liquids 360 (2022) 119426

Contents lists available at ScienceDirect

Journal of Molecular Liquids

journal homepage: www.elsevier.com/locate/molliq

Structure-property relationships in actinide containing molten salts – A review: Understanding and modelling the chemistry of nuclear fuel salts

A.L. Smith

Delft University of Technology, Faculty of Applied Sciences, Radiation Science & Technology Department, Mekelweg 15, 2629 JB Delft, The Netherlands

ARTICLE INFO

Article history:
Received 31 January 2022
Revised 13 May 2022
Accepted 18 May 2022
Available online 21 May 2022

Keywords:
Molten salts
Actinide halides
Structure
CALPHAD
Density
Viscosity

ABSTRACT

Molten salts have recently received increased attention worldwide as key materials for sustainable and low-carbon energy supply technologies (e.g. thermal energy storage, concentrated solar power technologies, fission and fusion nuclear reactors) thanks to their appealing thermo-physical properties. In particular, they are used as fuel and coolant in the Molten Salt Reactor (MSR), considered a breakthrough technology for the next generation of nuclear fission reactors. This review focuses on the thermochemical and thermo-physical properties of actinide bearing fluoride and chloride salts, used as nuclear fuel in MSRs, and more specifically on the structure–property relationships. In the last 15 years, the knowledge on the structural properties of actinide containing salts has grown quite significantly thanks to the development of dedicated high temperature in situ X-ray Absorption Spectroscopy measurements, and to the advancement of atomistic simulations. These have evidenced the formation of short-range order in the liquid, which contributes to storing energy in the salt and directly influences transport and thermodynamic excess properties. This interrelationship is illustrated in the present article, which covers both experimental and computational information, as well as most recent developments in the modelling methods at the mesoscale of the structural, thermodynamic, density and viscosity properties using the CALPHAD methodology.

Contents

E-mail address: a.l.smith@tudelft.nl

https://doi.org/10.1016/j.molliq.2022.119426
0167-7322/

1. Introduction

In view of the energy challenges of the 21st century, and the need to reduce greenhouse gas emissions, the development of sustainable and clean energy technologies has become a necessity. This requires innovative and ingenious materials with appealing thermo-physical properties. In this context, the interest for molten salts is growing rapidly, whether used for thermal energy storage (TES) systems, concentrated solar power (CSP) technologies, fission or fusion reactors [1,2]. Because of their advantageous properties (i.e low melting and high boiling points, low vapour pressure, thermal stability, high heat capacity and thermal conductivity, low viscosity, and in the case of nuclear applications low neutron capture cross-section, stability under irradiation, good fission product retention capabilities [1,2]), molten salts can be used as coolant, heat transfer fluid or heat storage medium depending on the particular application. They have in particular been considered for the primary and secondary coolants of nuclear reactors, more specifically for Molten Salt Reactors (MSRs) and Advanced High Temperature Reactors (AHTRs) [1], as well as for fusion systems [3]. They can serve as sensible heat or latent heat systems in TES technologies with applications in power generation, industrial process heat, vehicles, space heating and cooling [2]. They are also a suitable medium for advanced electrochemical recycling of spent fuel, pyroprocessing for extraction and purification of metals, zirconium alloy production [4], heat treatment of industrial components, or electrolytes for fuel cells and molten metal batteries [1].

Several classes of molten salts have been considered depending on the application: fluorides, chlorides, nitrates, fluoborates [1,2,5,6], and their suitability for a particular field of application has been quantified by so-called Figures of merits (FOMs) [7]. The FOMs are useful generalized heat-transfer metrics to compare the suitability of a salt medium depending on the nature of the flow, by accounting for its performance in terms of multiple physico-chemical properties simultaneously, more specifically the density, viscosity, thermal expansion, heat capacity, and thermal conductivity. This review focuses on the use of molten salts in the nuclear field, more specifically in Molten Salt Reactor technology and for electrochemical recycling of spent fuel, where fluorides and chlorides are to this date the two main candidates.

Historically, the development of molten salt technology goes back to the studies at the Oak Ridge National Laboratory (ORNL) in the period 1940s to 1970s with the Aircraft Reactor Experiment (ARE) [8], followed by the Molten Salt Reactor Experiment (MSRE) in the 1950s and 1960s [9]. Development stopped in the 1970s due to the limited technology readiness level, but MSR technology has regained interest as breakthrough technology, ideally suited for sustainable and low-carbon energy supply. The Molten Salt Reactor (MSR) [10,11] provides not only an innovative concept, but also an inherently safe design that remains subcritical in an accidental event or temperature increase [5]. Furthermore, it can be coupled to a thorium fuel cycle, which leads to less long-lived radioactive waste, and ensures a sustainable nuclear energy production (thorium resources on Earth being three times larger than uranium) [10]. Numerous nuclear technology companies and consortia are, at the time of writing of this article, developing MSR concepts worldwide at an intense rate (e.g. Terrestrial Energy, ThorCon, Flibe Energy, TerraPower, Seaborg Technologies, Moltex Energy, Kurchatov Institute, BARC, SAMOFAR and SAMOSAFER consortia etc.) [5].

The liquid nature of the fuel in the MSR design (a fluoride or chloride salt of typical composition e.g. ^{7}LiF-ThF_4-UF_4-PuF_3 for the European Molten Salt Fast Reactor (MSFR) [12] or NaCl-$MgCl_2$-UCl_3-$PuCl_3$ for the fast breeder molten salt reactor [13]) makes it unique among the current and next generation nuclear reactor concepts. One main challenge for the development of this technology and its commercialisation in the near future is a thorough understanding and modelling of the liquid fuel physico-chemical properties, i.e., density, viscosity, heat capacity, thermal conductivity, and vapour pressure. The salts used in MSRs are multi-component systems made of three or more end-members, showing complex non-ideal thermodynamic behaviour at the high temperatures used in the reactor (550–800°C [5]). Moreover, the chemical composition of the fuel continuously changes due to the fission process, introducing new reactive dissolved, precipitated or gaseous species, depending on local thermodynamic conditions, the so-called fission products. The reactor operation and its safety analysis require an exhaustive assessment, and fundamental understanding of the fuel chemistry and physico-chemical properties, as well as models and computer simulation codes predicting performance under normal operation and accidental conditions.

Despite being very promising, the available knowledge on the physico-chemical properties of molten salts is still far from complete. The experimental data are limited in some cases due to the challenges inherent to the work with molten salt materials, which are hygroscopic, highly corrosive at high temperatures, and in the case of nuclear applications radioactive. Nevertheless, over the last 20 years, a large thermodynamic database has been developed for fluoride and chloride molten salts based on the CALPHAD (CALculation of PHAse Diagrams) methodology and the quasichemical model in the quadruplet approximation [14]. In parallel, a number of atomistic simulations including molecular dynamics (MD), density functional theory (DFT), ab initio molecular dynamics (AIMD), and machine-learning potentials MD have been reported on the thermodynamic and transport properties of the salts [15,16,7,17], which are very valuable given the difficulties associated with the experimental studies [18].

A number of recent reviews can be cited on the available physico-chemical properties on molten salts for nuclear applications by Beneš and Konings [5], Capelli and Konings [6], or Beneš and Soucek [19]. The present review is dedicated to a subject that has not been covered at length in the aforementioned works, namely the structure–property relationships in molten salts for nuclear applications. The number of studies dedicated to the structure properties of the salts are not as numerous as other properties such as phase diagram equilibra for instance, due to the associated experimental challenges. The molten salts are ionic liquids where cations and anions form a loose network. Depending on conditions of composition, temperature and concentration, they can form a dissociated ionic melt, molecular species or exhibit oligomerization/polymerization [20,21]. The formation of short

Table 1
Crystallographic data on the most stable actinide fluorides and chlorides. CN(An) is the coordination number of the actinide in the AnX_n polyhedra.

Compound	Symmetry	Space group	Unit cell volume (Å^3)	CN(An)	$R_{ave}[An-X]$ (Å)	Ref.
Tetravalent actinide fluorides - ZrF_4 structure						
ThF_4	monoclinic	$C2/c$ (15)	986.4	8	2.324(19)[a]	[18]
ThF_4	monoclinic	$C2/c$ (15)		8	2.30(1)[c]	[18]
UF_4	monoclinic	$C2/c$ (15)	932.4	8	2.28(2)[a]	[33]
NpF_4	monoclinic	$C2/c$ (15)	911.2	8	2.26[a]	[33]
PuF_4	monoclinic	$C2/c$ (15)	890.6	8	2.25[b]	[34]
AmF_4	monoclinic	$C2/c$ (15)	873.8	8	2.23[b]	[34]
Tetravalent actinide chlorides						
α-$ThCl_4$	tetragonal	$I4_1/a$ (88)	530.7	8	2.87[b]	[26]
β-$ThCl_4$	tetragonal	$I4_1/amd$ (141)	539.5	8	2.83[b]	[35]
UCl_4	tetragonal	$I4_1/amd$ (141)	515.6	8	2.77[b]	[36]
$NpCl_4$	tetragonal	$I4_1/amd$ (141)	507.5	8	2.76[b]	[35]
Trivalent actinide fluorides - LaF_3 structure						
UF_3	hexagonal	$P\bar{3}c1$ (165)	327.9	9	2.49[b]	[31]
NpF_3	hexagonal	$P\bar{3}c1$ (165)	321.0	9	2.48[b]	[31]
PuF_3	hexagonal	$P\bar{3}c1$ (165)	316.3	9	2.46[b]	[12]
AmF_3	hexagonal	$P\bar{3}c1$ (165)	313.4	9	2.49[b]	[32]
Trivalent actinide chlorides - $LaCl_3$ structure						
UCl_3	hexagonal	$P6_3/m$ (176)	207.4	9	2.93[b]	[30]
$NpCl_3$	hexagonal	$P6_3/m$ (176)	203.7	9	2.91[b]	[37]
$PuCl_3$	hexagonal	$P6_3/m$ (176)	200.9	9	2.90[b]	[38]
$AmCl_3$	hexagonal	$P6_3/m$ (176)	199.6	9	2.89[b]	[39]

[a] Neutron diffraction data.
[b] X-ray diffraction data.
[c] EXAFS data.

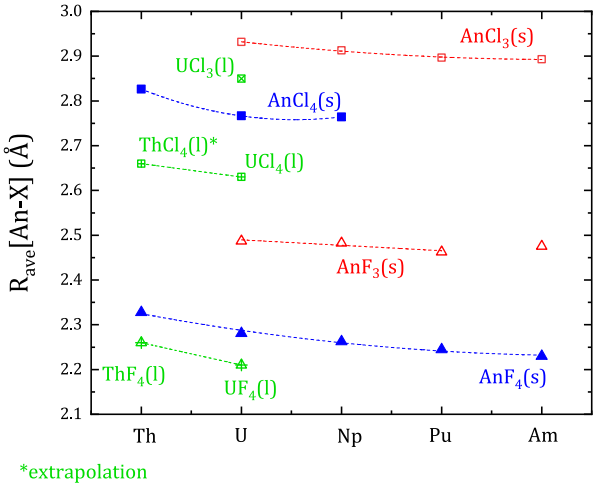

Fig. 1. Evolution of the mean An-X distance (An = Th, U, Np, Pu, Am; X = Cl, F) in the AnX_8 and AnX_9 polyhedra in the tetravalent and trivalent actinide fluorides and chlorides, both in the solid state (marked as "s") and in the liquid state (marked as "l"). Most probable distances are shown in the liquid state.

range order in the liquid contributes to storing energy in the salt and to thermodynamic excess properties as will be covered in more detail in this article. It can also be directly related to the transport properties. A striking example is that of a {LiF + BeF_2} mixture, that forms a dissociated melt (Li^+, BeF_4^{2-} and F^- species) at low BeF_2 content, and $Be_2F_7^{3-}$, $Be_3F_{10}^{4-}$, $Be_4F_{13}^{5-}$ and higher degree polymers with increasing BeF_2 content. This chemical speciation can be directly related to the viscosity of the salt mixture, which increases drastically with increasing BeF_2 content [15,16,20].

An extensive review of the structural properties of various molten metal halides was reported in 2011 by Rollet and Salanne [22]. However, at that time, the data available on actinide metal halides was limited to UCl_3 based on neutron diffraction (ND), X-ray diffraction (XRD), and molecular dynamics data, and $ThCl_4$ based on Raman spectroscopy data [22]. The behaviour of other actinide halides could only be predicted by analogy with rare earths as analogues for actinides in the + 3 oxidation state, and zirconium for actinides in the + 4 oxidation state. Since the latter review, a number of experimental studies including X-ray Absorption Spectroscopy (XAS), neutron diffraction, Nuclear Magnetic Resonance (NMR) or computational methods have been reported. We will thus scrutinize herein the properties and trends of the trivalent and tetravalent actinide bearing salts (i.e. the most stable oxidation states in MSR fuel mixtures[1] [6]) based on the latter data, with a more particular focus on mixtures envisaged and relevant in the current MSR reactor designs (e.g. mixtures of alkali metal halides with actinide halides, mixtures including beryllium fluoride or magnesium chloride). Next, the thermodynamic excess properties, more particularly mixing enthalpy data available on the same systems will be reviewed, and the relationship with the structure properties will be pointed out. The link to other thermo-physical properties such as density and viscosity will also be briefly illustrated. Finally, the most recent developments in the modelling methods of the structural, thermodynamic, density and viscosity properties will be addressed, with again an emphasis on the coupling between the various properties.

2. Structural properties of the actinide halides in the solid state

Before we dive into the structural properties of the melts, it is very instructive to consider the properties in the solid state. The crystal structures of the tetravalent and trivalent actinide fluorides and chlorides are reported in Table 1, including the reported symmetry, space group, unit cell volume at room temperature derived from X-ray or neutron diffraction data, coordination number of the AnX_n polyhedra (An = Th, U, Np, Pu, Am; X = F, Cl) in the structure, and average actinide-halide distance $R_{ave}[An-X]$ in those polyhedra. The evolution of $R_{ave}[An-X]$ as a function of the actinide cation is also shown in Fig. 1.

The tetravalent actinide fluorides AnF_4 show a monoclinic structure, in space group $C2/c$, isostructural with ZrF_4 and CeF_4. The actinide cation is found on two different crystallographic sites, both eightfold coordinated. The average An-F distance of the

[1] For an overview of all possible oxidation states of the actinide chlorides and fluorides, see [6].

AnF_8 polyhedra on those two sites differ by no more than 0.024 Å. The AnF_8 polyhedra moreover share corners, forming a three-dimensional network structure. The average An-F distance varies from 2.33 Å for Th to 2.23 Å for Am. For future reference, and comparison with bond distances in the liquid state, the corresponding average Zr-F distance in ZrF_4 is equal to 2.10 Å [23], while that in CeF_4 is equal to 2.24 Å [24]. Those values are in line with the series of the actinide tetrafluorides, when considering the Shannon ionic radii [25] of Zr^{4+} and Ce^{4+} in 8-fold coordination (0.84 and 0.97 Å, respectively), compared to those of Th^{4+}, U^{4+}, Np^{4+}, Pu^{4+} and Am^{4+} (1.05, 1.0, 0.98, 0.96, 0.95, respectively).

The tetravalent actinide chlorides $AnCl_4$ are stable in the form of a tetragonal structure, in space group $I4_1/amd$. The actinide cation is again eightfold coordinated, but on a single crystallographic site. The $AnCl_8$ polyhedra share edges, forming infinite chains in the *a* and *b* directions. The average An-Cl distance varies between 2.83 Å for Th and 2.76 Å for Np. It should be noted that $ThCl_4$ is reported to have a polymorphic transition between a low temperature metastable α phase (tetragonal in space group $I4_1/a$) stable below 678 K [26], and a high temperature β modification (tetragonal, in space group $I4_1/amd$). The reported thermodynamic data usually refers to the latter phase, which is the one observed experimentally [27]. The α-β phase transition is in particular not reported in phase diagram investigations of systems such as NaCl-$ThCl_4$ [27] or $PuCl_3$-$ThCl_4$ [28]. Mason et al. only managed to observe the low-temperature modification by using a very slow cooling rate [26].

The trivalent actinide fluorides AnF_3 adopt a hexagonal symmetry, in space group $P\bar{3}c1$, isostructural with some of the rare-earth halides, namely LaF_3, CeF_3 and NdF_3 [6,29]. It is worth noting that the reported crystal structure for UF_3 in the literature is hexagonal in space group $P6_3cm$, however. The corresponding works date back from the 1950s and 1960s [29], and 2018 for one more recent study outlying a "facile" synthesis method for UF_3 [30]. But the reported U-F average distance with the $P6_3cm$ symmetry is not in line with the rest of the actinide trifluoride series. In view of the expected isostructurality with the other actinide trifluorides, one can suspect UF_3 to also adopt the $P\bar{3}c1$ symmetry. The distance shown in Fig. 1 is derived from a refinement made using the latter space group (unpublished) on data provided by the Joint Research Centre of the European Commission (JRC Karlsruhe) [31]. Similarly the refined distances for NpF_3 (unpublished) were also derived from the refinement of data provided by the JRC Karlsruhe. The data for PuF_3 and AmF_3 are from [12,32], respectively. The actinide cation in the $P\bar{3}c1$ structure is ninefold coordinated, and the AnF_9 polyhedra share edges. The average An-F distance varies between 2.49 Å for U and 2.46 Å for Pu. The distance for the Am salt (2.49 Å), taken from a study dating back to 1983 [32], is slightly higher than the rest of the U-Np-Am series of trifluorides, and should probably be re-visited.

Finally, the actinide trichlorides $AnCl_3$ form a hexagonal structure, in space group $P6_3/m$, isostructural with some of the rare-earth halides, namely $LaCl_3$, $CeCl_3$, $NdCl_3$ and $GdCl_3$ [29]. The actinide cation is again ninefold coordinated and the $AnCl_9$ polyhedra share edges. The average An-Cl distance varies between 2.93 Å for U and 2.89 Å for Am.

When looking at general features in Fig. 1, one can point out the shortening of the average An-X distance along the series of the actinide elements (from Th to Am) as expected from the contraction of the ionic radius, and the higher average An-Cl distances compared to the An-F distances, which is related to the larger size and polarizability of the chloride compared to the fluoride anion.

3. Local structure properties in the liquid state

The local structure properties as discussed hereafter have been investigated using a combination of experimental techniques, including in situ high temperature Extended X-ray Absorption Fine Structure (EXAFS) spectroscopy, Raman spectroscopy, X-ray diffraction (XRD) and neutron diffraction (ND), as well as atomistic simulations, including semi-classical molecular dynamics (MD) using the Polarizable Ion Model (PIM) [40], ab initio molecular dynamics (AIMD), and Density Functional Theory (DFT). We refer the reader to the review of Rollet and Salanne [22] and more specialized reference works for a detailed explanation of those techniques. We will simply mention briefly some of the concepts often referred to in this article.

The interpretation of the structure of a liquid involves looking at the so-called radial distribution function (RDF) or pair correlation function, noted $g(r)$. $g(r)$ is the probability density function describing the likelihood of finding a particle in a shell of thickness *dr* at a distance *r* from a central particle. In other words, it describes the variation of the local number density around the particle of interest. Partial RDFs $g_{AB}(r)$ are usually considered, that correspond to the distribution of one particle *B* around a particle *A*[2]. The total number of particles *B* surrounding a central particle *A* within a sphere of radius $r\prime$ is then obtained by integrating with the following formula:

$$N_B(r\prime) = 4\pi\rho_B \int_0^{r\prime} g_{AB}(r) r^2\, dr \tag{1}$$

where $N_B(r\prime)$ is the total number of particles *B* within a sphere of radius $r\prime$ of the RDF, and ρ_B is the number density in *B* particles.

Of more interest in this article, is the coordination number of the first coordination shell (also called solvation shell) around a central particle *A*. This is given by:

$$CN_B = 4\pi\rho_B \int_0^{r_{min,1}} g_{AB}(r) r^2\, dr \tag{2}$$

where CN_B is the coordination number of particles *B* around a central particle *A*, $r_{min,1}$ is the first minimum in $g(r)$ called bond cut-off distance, and ρ_B the number density in *B*[3].

This means that any atom *B* closer to *A* than the minimum of the RDF belongs to the first coordination shell. The partial RDFs are also used to characterize the distribution of *A*-*B* distances. In particular, the first maximum of the *A*-*B* RDF denotes the most probable distance between *A* and *B* (usually the one quoted in most articles), while the expected distance $E[R]$ is given by the following formula:

$$E[R] = \frac{\int_0^{r_{min,1}} rg(r)\, dr}{\int_0^{r_{min,1}} g(r)\, dr} \tag{3}$$

Finally, a more extended picture of the local structure up to intermediate-range is also obtained from the partial RDFs. If the maximum of the *A*-*A* RDF is less than twice the *A*-*B* distance, then there is indication of a *A*-*B*-*A* linkage, and more generally of the formation of chains of connected *A* particles in the melt.

Among the various computational methods used to study the structure of molten salts, molecular dynamics simulations using the Polarizable Ion Model (PIM), have been especially used extensively and will be mentioned a number of times in this article. The Polarizable Ion Model was developed by Madden and co-workers and is particularly well-suited for the simulation of chloride and fluoride salts [41,40]. The approach is semi-classical in the sense that the interaction potentials between given pairs of ions are first derived from ab initio calculations on the condensed phases [41]. They include both classical interaction forces, i.e. charge-charge V_{qq}, repulsion V_{rep}, dispersion V_{disp} and forces resulting from polarization effects V_{pol} [40]. We refer the reader to the cited articles or

[2] Note that $g_{AB}(r)$ and $g_{BA}(r)$ are the same function.
[3] Note that CN_B usually differs from CN_A.

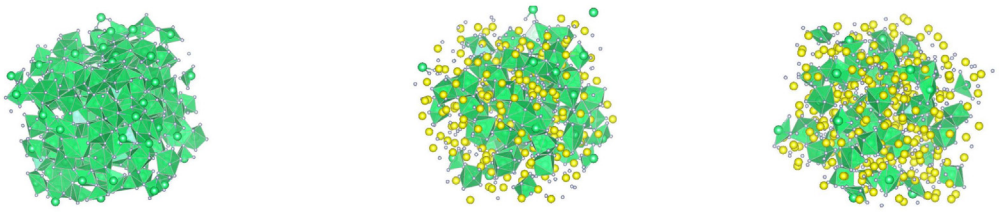

(a) ThF_4 (b) $(LiF:ThF_4) = (0.75:0.25)$ (c) $(LiF:ThF_4) = (0.85:0.15)$

Fig. 2. MD snapshot of molten (a) ThF_4 (b) $(LiF:ThF_4) = (0.75:0.25)$ and (c) $(LiF:ThF_4) = (0.85:0.15)$. ThF_n polyhedra are shown in green, Li cations in yellow and fluoride anions in grey.

Table 2
Local structure properties of molten actinide halides. Uncertainties, when available, are indicated in parenthesis. "An" stands for actinide, i.e. Th or U. "X" stands for fluorine or chlorine. The data for UCl_3 in italic are shown for completeness but discarded in this review.

Compound	T(K)	CN(An)	$R_{ave}[An-X]$	$[AnX_n]^{4-n}$ fraction						Ref.
Tetravalent actinide fluorides				$[AnF_5]^-$	$[AnF_6]^{2-}$	$[AnF_7]^{3-}$	$[AnF_8]^{4-}$	$[AnF_9]^{5-}$	$[AnF_{10}]^{6-}$	
ThF_4	1433	7.92	2.34*/ 2.26**		0.034	0.262	0.473	0.210	0.021	[21][a]
	1433	8.0(8)	2.32(1)*							[21][b]
	1433	8.09			0.005	0.205	0.511	0.251	0.028	[42][a]
UF_4	1357	7.94	2.28*/ 2.21**		0.023	0.250	0.509	0.201	0.018	[21][a]
	1357	8.0(7)	2.27(1)*							[21][b]
Tetravalent actinide chlorides				$[AnCl_5]^-$	$[AnCl_6]^{2-}$	$[AnCl_7]^{3-}$	$[AnCl_8]^{4-}$	$[AnCl_9]^{5-}$	$[AnCl_{10}]^{6-}$	
$ThCl_4$	1073	~6	2.66***							[43][c]
UCl_4		6.1	2.63**	0.18	0.60	0.2	0.02			[44][d]
Trivalent actinide chlorides				$[AnCl_5]^{2-}$	$[AnCl_6]^{3-}$	$[AnCl_7]^{4-}$	$[AnCl_8]^{5-}$	$[AnCl_9]^{6-}$	$[AnCl_{10}]^{7-}$	
UCl_3	*1200*	*6*	*2.84*							[45][g,h]
	1113	*6*	*2.84*							[46][f,h]
		7.05	2.82							[47][f]
	1200	8	2.85							[48][e]
	1200	8.1	2.85							[48][a]
	1200	6.8	2.74		~0.4	~0.4	~0.18			[44][d]
	1200	7.69	2.78		0.0732	0.332	0.432	0.150	0.0126	[49][a]
	1200	7.2	2.84							[17][d]

[a] MD data using the PIM. MD trajectories were used as input for the FEFF8.40 [50] *ab initio* code to simulate to EXAFS spectra and compare directly with the experimental data as done by various groups in recent years [51,52,18,21] for liquids that are highly disordered systems and show anharmonic behaviour and high Debye–Waller factors.
[b] Fitting of EXAFS data using the standard equation for solids.
[c] Raman data.
[d] Ab-initio molecular dynamics (AIMD).
[e] X-ray diffraction (XRD).
[f] Neutron diffraction (ND).
[g] Classical MD.
[h] Data discarded in this review.
* Expectation value.
** Peak maximum of the RDF (most probable distance).
*** Extrapolation.

to the review of Rollet and Salanne [22] for a more detailed explanation of the different terms.

3.1. Pure actinide halides

The local structural properties of ThF_4 and UF_4 have been recently scrutinized by Ocádiz Flores et al. using in situ high temperature EXAFS spectroscopy [21] and by Dai et al. for ThF_4 using molecular dynamics with a polarizable force field model [42]. Molten ThF_4 and UF_4 can be described as a network of $[AnF_n]^{4-n}$ (An = Th, U; n = 6, 7, 8, 9, 10) polyhedra that share corners (~69–70%), edges (~27%) and faces (~3–4%) [42,21] (Fig. 2a). The coordination numbers and average Th-F and U-F distances in the $[AnF_n]^{4-n}$ structural units are listed in Table 2.

The dominant species are 7-, 8- and 9-coordinated complexes, $[ThF_8]^{4-}$ and $[UF_8]^{4-}$ being the predominant species. The average coordination number is also very close to 8 in both cases. The local coordination environment is thus preserved when transitioning from the solid (see Section 2) to the liquid state. The average An-F distance is very similar or slightly shorter than in the solid state as reported by Ocádiz Flores et al. [21], depending if one considers the most probable or expected distance. For comparison, the Th-F distance is 2.324(19) Å in the solid state [18] and 2.34/2.32(1) Å in the liquid state (expectation value, the most probable distance shown in Fig. 1 being 2.26 Å). The U-F distance is 2.28(2) Å in the solid phase [33] compared to 2.28/2.27(1) Å in the liquid state (expectation value, the most probable distance shown in Fig. 1 being 2.21 Å). A strengthening of the local structure is observed upon melting: although longer bond lengths can form compared to the solid, shorter ones close to the most probable distance become at the same time more populated [21,53]. Dai et al. moreover studied the evolution of the coordination numbers of molten ThF_4 in the range 1273–1733 K, which display a decrease of the contributions of the 8-fold and 9-fold coordinations with increasing temperature, and a concordant increase in the 6-fold, 7-fold and 10-fold complexes [42]. The distribution of 6-, 7-, 8- and 9-fold coordinated species is equivalent at 1733 K (23, 26.2, 23.8 and 16.9%, respectively). The average coordination number varies from 8.1 at 1273 K to 7.6 at 1733 K. This can be related to various factors, namely a decrease in density, increased thermal disorder and faster exchange rates of the fluoride anions in the solvation shell.

It is interesting the compare those data with the local structure of the isostructural compound ZrF_4, scrutinized by Alders et al. using MD and the PIM model [54]. The sevenfold coordinated complex $[ZrF_7]^{3-}$ is the most abundant (49.8% at 1400 K), followed by $[ZrF_6]^{2-}$ (26.4%) and $[ZrF_8]^{2-}$ (20.8%). The average coordination number is 6.96, i.e. lower than in ThF_4 and UF_4 melts, and average Zr-F distance is 2.01 Å (most probable distance), compared to 2.10 Å in the solid state [23]. There also, a strengthening of the local structure is thus observed upon melting. The lower Zr-F average distance and lower coordination number are related to the smaller ionic radius of Zr^{4+}.

Photiadis and Papatheodorou performed high temperature Raman spectroscopy measurements of molten $ThCl_4$ in 1999 [43], which suggested the occurrence of edge-sharing thorium octahedra units $[ThCl_6]^{2-}$, leading to the formation of $Th_2Cl_{10}^{2-}$, $Th_3Cl_{14}^{2-}$, $Th_3Cl_{10}^{2+}$ etc. chains of small length. The authors justified the presence of such ionic species in relation with the ionic conductivity of $ThCl_4$. Liu et al. reported MD simulations with the PIM model on LiCl-$ThCl_4$ mixtures with compositions in the range 4.85–66.7% $ThCl_4$ [55]. More detail on the coordination chemistry in the mixtures is given in the next section. Although the corresponding study does not cover pure $ThCl_4$, we can tentatively extrapolate the behaviour from the highly concentrated solutions. The Th-Cl distance obtained from the RDFs is 2.66 Å, with little variation with the $ThCl_4$ concentration. In particular, the formation of a network with bridging chlorides as proposed by Photiadis and Papatheodorou is confirmed. Moreover, the predominant complex is found to be $[ThCl_6]^{2-}$, in accordance with the Raman studies. The bridging mechanism at high concentrations is dominated by edge-sharing, followed by face-sharing. The lower coordination number in $ThCl_4$ (∼6) compared to ThF_4 (∼8) is related to the smaller ionic radius of F^- compared to Cl^-: the higher the ratio of the cation/anion ionic radius is, the larger the coordination number is expected to be. This leads to more bridging fluorides than chlorides in the network structure, thus the $ThCl_4$ structure is "weaker". Further investigations of the local structure of molten $ThCl_4$ using experimental techniques (e.g. EXAFS, neutron diffraction) and simulations would be extremely useful in view of the growing interest and technological benefits in the use of a NaCl-$ThCl_4$-$PuCl_3$ [56] fuel mixture for fast spectrum chloride reactors.

It seems that no experimental studies have been reported to this date on the structural properties of molten UCl_4. Li et al. reported first-principles molecular dynamics simulations on this system, however [44]. As for the molten $ThCl_4$ salt previously considered, 6-fold coordinated species $[UCl_6]^{2-}$ were found predominant. The average U-Cl distance was found around 2.63 Å, which is about 0.4 Å higher than in molten UF_4 and 0.14 Å lower than in solid UCl_4. A network of bridging chlorides is again observed with 99% of U in a polymer chain and only 1% of U in isolated complexes [44].

A number of studies have been reported on UCl_3, both experimental (using high temperature X-ray and neutron diffraction) and computational (using classical and first-principles MD). The earlier studies by Okamoto et al. (1998) [45] and Neilson et al. [46] using XRD and ND, respectively, report a lower coordination number (∼6) compared to the later studies by Adya et al. (1999) [47], Okamoto et al. (2005) [48], Li et al. [44], Nguyen et al. [17], and van Oudenaren et al. [49] that found higher coordination numbers, around 6.8–8.1, using ND, XRD, AIMD, PIM-MD and machine learning potentials. It is clear that there is still no clear consensus on the coordination geometry. The same XRD data were analysed in the two works of Okamoto et al. [45,48], and interpreted with the aid of molecular dynamics simulations. The study in 1998 made use of classical MD potentials, more specifically an ionic Busing-type potential and a covalent Morse potential. This work showed that a fully ionic model was not appropriate to represent the local structure, and that a much better agreement was obtained when introducing some degree of covalency into the U-Cl bond. The subsequent study in 2005 was based on simulation of the XRD with the polarizable ion model, where polarization effects of Cl^- were accounted for. The resulting coordination was found very close to 8, in good agreement with the later studies. The latter coordination is thus retained for molten UCl_3. The U-Cl average bond distance is around 2.78–2.85 Å depending on the technique used for the assessment. The AIMD method seems to underestimate this distance slightly. In any case, it is clear that network formation/oligomerization also takes place, and corner-sharing was reported to be the dominant mechanism [44].

No data seem to be available to this date on molten UF_3, neither from experimental nor computational work. This would be extremely valuable given that UF_3 is added in small amounts to the fuel salt mixture in some designs (typically with a UF_4/UF_3 ratio around 100 [5]) to set the redox potential to acceptable values and limit the corrosion of structural materials.

Thus, from this analysis we see that the tetravalent actinide fluorides ThF_4 and UF_4 adopt a 8-fold coordination, while the equivalent tetrachlorides $ThCl_4$ and UCl_4 are stable on average in 6-fold coordination, which is related to the smaller ionic radius of the fluoride compared to the chloride anion. The larger coordination number in ThF_4/UF_4 also leads to more bridging fluorides in the network structure, thus the actinide chloride structures are slightly "weaker". Trivalent chloride UCl_3 is stable in 8-fold coordination according to the most recent studies. The actinide-halide distance in the molten state is generally shorter than in the solid state by about 0.07–0.14 Å (Fig. 1), which indicates a strengthening of the local structure.

Finally, it is interesting to point out some features related to the change in oxidation state of the actinide cation. Li et al. looked at the effect of the valence state in UCl_3/UCl_4 in mixtures with NaCl [44]. One of the main observations was that the first coordination shell of the chloride anion was more dynamic in the trivalent compared to the tetravalent mixtures, which translates to weaker bonds (faster dissociation) in UCl_3 salt. The maxima of the free-energy barriers for the U^{4+}-Cl^- and U^{3+}-Cl^- dissociations were calculated to be 59 kJ·mol^{-1} and 43 kJ·mol^{-1} at $x(UCl_4)$ = 0.32 and $x(UCl_3)$ = 0.25 in mixtures with NaCl, respectively. At the same time, the authors report a higher tendency for network formation in UCl_3 compared to UCl_4 salt, which leads to higher coordination numbers (∼6 in UCl_4 and ∼8 in UCl_3).

3.2. Alkali metal-actinide halide binary mixtures

A number of alkali metal-actinide halide mixtures have been investigated in the literature using Raman spectroscopy, EXAFS and molecular dynamics simulations. An overview of available data with the corresponding references is given in Tables 3 and 4. We will not describe every system in detail in this review, but will rather point to the trends encountered across these systems. We refer the reader to the cited papers for further details on a specific system.

LiF-ThF_4 appears as the most studied system, which is due to its technological importance. For thorium (resp. uranium) fluoride-alkali fluoride systems, the distribution of $[AnF_n]^{4-n}$ (An = Th, U) complexes ranges between 6 and 10 [21,60], the 7-fold, 8-fold and 9-fold complexes being the most abundant for Li, Na, and K. For cesium which is found at the end of the alkali-metal series, the contributions from 6-fold, 7-fold and 8-fold clusters are the most predominant, with an average coordination number that reaches 6.2 at $x(AnF_4)$=0.25 [21]. As for thorium chloride systems, the Raman studies of Photiadis and Papatheodorou suggested the

Table 3
Overview of the investigated binary alkali metal-actinide fluoride mixtures by various experimental and computational techniques. "nr": not reported. "An": actinide, i.e. Th or U. CN(An) indicates the coordination number of fluoride anions around the actinide cation.

System	$x(AnX_4)$	T(K)	CN(An)	Technique	Ref.
LiF-ThF_4	0.1,0.25,0.50	1133,973,1193	7.88,7.73,7.78[a]	EXAFS/PIM	[21]
	0.18,0.25,0.35	973,973,973	8.05,7.94,8.06[a]	EXAFS/PIM	[57]
	0.05,0.10,0.15,0.18,0.20,0.23	1115,1070,1015,970,970,855	8,7.99,8.02,8.05,7.95,8.10[a]	PIM	[57]
	0.25,0.30,0.35,0.40,0.50	875/970,855/970,970,1035,1135	8.09/7.94,8.20/8.03,8.06,7.98,7.87[a]	PIM	[57]
	0.05	1123/1173/1223/1273/1323/1373	8.0/7.9/7.8/7.8/7.7/7.7	PIM	[58]
	0.0485,0.1202,0.1988,0.3005	1200	7.86,7.82,7.82,7.8*	PIM	[53]
	0.4,0.5,0.6667	1200	7.84,7.87,7.96*	PIM	[53]
	0.05,0.35	1273,1273	7.86,7.69	PIM	[42]
	0.22	850/900/950/1000/1050/1100	8.13/8.07/8.0/7.98/7.95/7.87	PIM	[59]
NaF-ThF_4	0.33,0.50,0.67	1073,1108,1252	7.52,7.89,7.83[a]	EXAFS/PIM	[21]
	0.10*,0.46*,0.60*	1223,1223,1223	7.6,7.7,8.0*	EXAFS/PIM	[57]
	0.05	1123/1173/1223/1273/1323/1373	7.5/7.5/7.5	PIM	[58]
KF-ThF_4	0.167,0.33,0.50	1060,1123,1209	7.12,6.99,7.53[a]	EXAFS/PIM	[21]
	0.18,0.25	1073,1173	nr,7.03[a]/7.1[b]	EXAFS/PIM	[52]
	0.25,0.35,0.46	1073/1173,1073/1173,1073/1173	7.1/7.0,7.2/7.0,7.6/7.4*	EXAFS/PIM	[57]
	0.05	1273/1323/1373	7.1/7.0/7.0/7.0/6.9/6.9	PIM	[58]
CsF-ThF_4	0.25, 0.50	1301,1201	6.24,6.97[a]	EXAFS/PIM	[21]
LiF-UF_4	0.25,0.5,0.67	831,1040,1216	7.92,7.80,7.72[a]	EXAFS/PIM	[60]
	0.05,0.10,0.15,0.20	1175,1125,1075,1000	7.75,7.68,7.82,7.86	EXAFS/PIM	[57]
	0.274,0.30	825/875/925/975,875	7.90/7.91/7.85/7.86,7.89[a]	EXAFS/PIM	[57]
NaF-UF_4	0.50,0.67	1033,1153	7.75,7.76[a]	EXAFS/PIM	[21]
KF-UF_4	0.50,0.67	1098,1090	7.42,7.72[a]	EXAFS/PIM	[21]
	0.14	1073	nr	EXAFS/PIM	[52]
CsF-UF_4	0.25,0.50,0.67	1293,1058,1191	6.2,7.14,7.46[a]	EXAFS/PIM	[21]

[a] MD data using the PIM.
[b] Fitting of EXAFS data using the standard equation.
* Data extracted from a figure, but not tabulated in the corresponding paper.

Table 4
Overview of the investigated binary alkali metal-actinide chloride mixtures by various experimental and computational techniques. "nr": not reported. "An": actinide, i.e. Th or U. CN(An) indicates the coordination number of chloride anions around the actinide cation. "n.r" means not reported.

System	$x(AnX_n)$	T(K)	CN(An)	Technique	Ref.
LiCl-$ThCl_4$	0.1,0.2,0.25,0.33,0.5,0.77,1	873,873,873, 873, 923, 1003, 1073	n.r.	Raman	[43]
	0.0485,0.12,0.199,0.301,0.4	1200	6.5,6.6,6.6,6.6,6.7	PIM	[55]
	0.5,0.667	1200	6.7,6.7	PIM	[55]
NaCl-$ThCl_4$	0.2,0.25,0.33,0.5,0.75,0.82	993,993,993,923,993,1023	n.r.	Raman	[43]
	0.273	1070	6.5	AIMD	[17]
	0.273	700,800,900,1000,1070	7.3,7.3,7.1,7.0,6.5	GAP-MD	[17]
KCl-$ThCl_4$	0.1,0.2,0.25,0.33,0.5,0.75,0.85	993,973,993,973,973,1003,1023	n.r.	Raman	[43]
CsCl-$ThCl_4$	0.05,0.1,0.25,0.33,0.45,0.5	973,973,1013,973,1023,973	n.r.	Raman	[43]
	0.75,0.87,1	973,1023,1233	n.r.	Raman	[43]
LiCl-UCl_3	0.2,0.8	n.r.	n.r.	ND	[47]
NaCl-UCl_4	0.5	1200	6.1	AIMD	[61]
	0.1,0.25,0.32,0.4,0.52,1	1200	6.71,6.17,5.97,5.99,6.02,6.07	AIMD	[44]
NaCl-UCl_3	0.5	1200	6.5	AIMD	[61]
	0.049,0.1,0.148,0.199,0.251	1100	6.17,6.38,6.61,6.69,6.83	PIM	[49]
	0.302,0.352,0.399,0.498	1100	6.98,7.06,7.23,7.39	PIM	[49]
	0.049,0.1,0.148,0.199,0.251	1400	6.23,6.33,6.36,6.46,6.58	PIM	[49]
	0.302,0.352,0.399,0.498	1400	6.66,6.77,6.87,7.04	PIM	[49]
	0.286	1345	7.1	AIMD	[17]
	0.286	945,1045,1145,1245,1345	7.8,7.63,7.4,7.2,7.0	GAP-MD	[17]
	0.05,0.1,0.15,0.2,0.25,0.3	1100	6.61,6.68,6.75,6.85,6.97,7.09	PIM	[62]
	0.35,0.4,0.45,0.5,0.55	1100	7.23,7.32,7.39,7.48,7.56	PIM	[62]
	0.1,0.25,0.3,0.4,0.54,1	1200	5.99,5.85,6.04,5.94,6.18,6.75	AIMD	[44]
	0.8	n.r.	n.r.	ND	[47]
KCl-UCl_3	0.8	n.r.	n.r.	ND	[47]
CsCl-UCl_3	0.8	n.r.	n.r.	ND	[47]

predominance of $[ThCl_6]^{2-}$ complexes in the melt in equilibrium with $[ThCl_7]^{3-}$ [43]. This was later confirmed in the molecular dynamics simulations of Liu et al. [55] of the LiCl-$ThCl_4$ system, where 6-fold coordinated complexes were found largely dominant across the whole composition range, followed by 7-fold and 5-fold coordinated complexes. The AIMD and GAP-MD (Gaussian approximate potential-molecular dynamics) simulations of Nguyen et al. on NaCl-$ThCl_4$ also gave average coordination numbers of 6.5–7.3 depending on temperature [17], and predominance of $[ThCl_7]^{3-}$ and $[ThCl_6]^{2-}$ complexes. In NaCl-UCl_4, the average coordination number is also around 6, while it is higher in NaCl-UCl_3 (ranging from 6.17 to 7.56 depending on temperature and composition).

A strong short-range ionic ordering is observed in the mixtures, with some degree of covalency in the first coordination shell, which leads to a rather deep minimum of the first peak of the calculated An-X RDFs by molecular dynamics methods [21]. We will discuss hereafter the trends (i) across the series of the alkali metal elements, (ii) as a function of the metal/actinide cation, (iii) as a function of temperature, (iv) as a function of composition within

a single system, (v) as a function of the halide anion (fluorine versus chlorine), (vi) as a function of the valence state of the actinide cation.

3.2.1. Trends across the series of alkali metals

When the size of the alkali metal increases (from Li to Cs), it is clear from the data in Table 3 that the average coordination number decreases. This is also accompanied by a decrease in the average An-X bond length (X = F, Cl) [58,57,21]. This can be related to the fact that AnX_n (An = Th, U; X = F, Cl; n = 3,4) salts qualify as Lewis acids that attract the anions (fluoride or chloride) from the alkali fluoride (resp. chloride) AX salt: for larger and more fluorobasic alkali cations, the An-X bonding is stronger leading to shorter bond lengths.

The increasing size of the alkali metal also leads to more stable complexes. This trend can also be seen when looking at so-called cage-out times of the An-X cage-out correlation functions calculated by molecular dynamics simulations, which are a measure of the lifetimes of the coordination complexes. The cage-out time is defined as the time required for the correlation function to reach a value of 1/e. The more stable a complex is, the longer its cage-out time will be. A comparison of the Th-F or Zr-F cage-out correlation functions in different alkali systems have shown that the cage-out time increases with the size of the alkali metal cation, indicating the formation of more stable clusters [51,58]. This can be explained by the larger distance between the complexes in solvents where the alkali metal has a larger ionic radius, which increases the energetic barrier required for a fluoride (resp. chloride) anion to leave a complex and enter another one [21].

3.2.2. Trends as a function of the metal/actinide cation

When looking at trends as a function of the metal (actinide or zirconium) cation, one sees that lower coordinations are obtained in the zirconium melts (mainly 6-, 7- and 8-coordinated complexes) compared to the actinide melts (mainly 7-, 8-, and 9-coordinated complexes). This can in turn be related to the basicity of the salt. The lower CNs in the Zr-based systems lead to more free fluoride F^- (resp. chloride) for a given composition, and thus to an increase of the fluorobasicity (resp. chlorobasicity) [57]. At the same time, the metal-fluoride (resp. chloride) distances are shorter (stronger bonds) [53] in the zirconium melt. This is particularly interesting considering that zirconium, thorium and uranium all have the same coordination environment in the solid state (see Section 2), with 8-fold coordinated cations in the monoclinic structure. When comparing the situation in the thorium melts compared to the uranium melts, one observes lower U-X distances than Th-X distances, in accordance with the actinide contraction [21,60], and the behaviour in the solid state.

3.2.3. Trends as a function of temperature

Little or rather limited variation is generally seen with temperature. The first solvation or coordination shell becomes a little "looser", as reflected by the evolution of the width of the first peak of the An-X RDF that becomes slightly broader, or by the cage-out times of the cage-out correlation functions [58]. The fraction of complexes with lower CNs increases, while the fraction of higher CNs complexes decreases, leading overall to a decrease of the average CN with increasing temperature. This is to be expected, as more thermal energy will lead to more disorder and faster exchange rates of the fluoride (resp. chloride) anions. As for the network formation described in the following section, it happens at a slightly lower rate with increasing temperature, which can be related to the decreasing density [49]. The evolution of the average An-An distance finally is not straightforward: the thermal expansion with temperature leads to increasing distance between the actinide cations in principle, but the concurrent lowering of the average CNs also results in stronger cation–anion interactions, thus to a decrease of the distance between actinide centers in a network structure.

3.2.4. Chemical speciation as a function of composition for a single system

The An-X distance (and the corresponding RDFs) shows little variation with composition. By contrast, the evolution is greater for the An-An bond, as illustrated in Figs. 3a and b for the LiF-ThF_4 system. The AnX_n (An = Th, U; n = 3,4) end-member is made of oligomers of corner, edge and face-sharing polyhedra as detailed in the previous section, while the alkali metal end-member is a fully dissociated melt (A^+ and X^- species). When the concentration of alkali metal increases, the AnX_n network is progressively broken, until only molecular complexes of the type $[AnX_n]^{4-n}$ and $[AnX_n]^{3-n}$ are stable at very low AnX_n content. Conversely, one observes a progressive oligomerization of the melt when going from the pure alkali melt melt to the actinide melt, with the successive formation of dimers, trimers, tetramers and higher order chains. Such evolution is illustrated in Fig. 4 for the LiF-ThF_4 system at T = 1121 K, using the PIM parameters reported in [21]. MD snapshots of the (Li,Th)F_x melt at various compositions, showing the progressive network formation when the ThF_4 content increases, are also shown in Fig. 2.

It is very instructive to investigate the critical composition above which chains of nuclearity greater than 3 (above trimers) start to form. We have plotted in Fig. 5 a simplified representation of the chemical speciation in LiF-MF_4 (M = Th, U, Zr), where only monomers, dimers and "polymers" are included. The monomers correspond to all $[ThF_n]^{4-n}$ units (n = 6, 7, 8, 9, 10), while the "polymers" correspond to trimers, tetramers plus all clusters with a nuclearity higher than 4. The polymeric units become predominant (with a fraction above 50%) around 18% UF_4, 18% ThF_4 and 38% ZrF_4, which shows a greater tendency towards network formation in the Th/U melts compared to the Zr melts. This is also related to the higher coordination numbers observed in the Th/U melts, leading to more bridging fluorides.

Similarly, the distribution is compared in AF-ZrF_4 melts at T = 1300 K [54,63] with (A = Li, Na, K) to judge the effect of the alkali cation (Fig. 6). This time, the predominance of the polymeric unit is observed above 36%, 38% and 40% in the LiF, NaF and KF melts, respectively. The higher tendency towards network formation for mixtures with smaller alkali cations is easily understood as the larger the alkali-metal is (with a larger ionic radius), the more stable isolated complexes will be, and the more easily any network will also be disrupted.

3.2.5. Trend as a function of the halide anion

The coordination numbers are generally lower in the chloride mixtures than in the fluoride mixtures, which is in line with the data presented in the previous section on the end-member compounds. Liu et al. [55] compared the cage-out correlation times in LiCl-$ThCl_4$ and LiF-ThF_4 melts, and found shorter lifetimes in the fluoride melt compared to the chloride melt (or shorter cage-out times), indicating less stable clusters. This is somehow counter-intuitive, as one would rather expect the shorter and stronger Th-F bonds to lead to more stable clusters. However, Liu et al. [55] stress that the cage-out times and calculated lifetimes do not only reflect the bonding strength, but more largely the characteristics of the formed structural network, i.e. the linkage sharing mechanism by either corner, edge or face sharing. The edge-sharing and more particularly face-sharing mechanisms were reported to decrease the stability by contrast with corner-sharing.

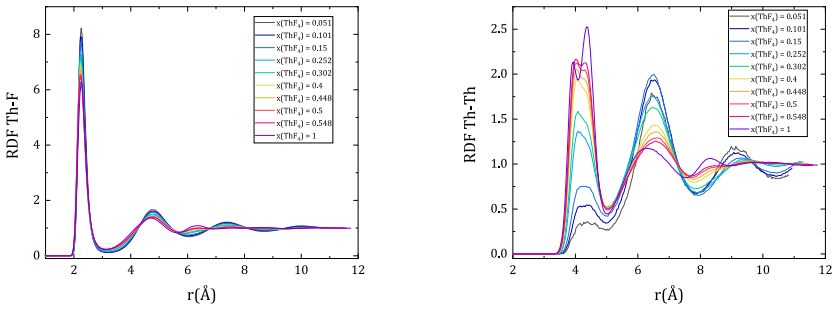

(a) RDF Th-F (b) RDF Th-Th

Fig. 3. Radial distribution functions in the LiF-ThF_4 system, calculated at T = 1121 K: (a) Th-F RDF and (b) Th-Th RDF.

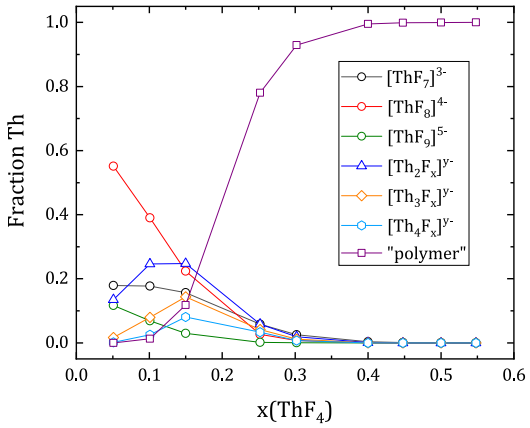

Fig. 4. Fraction of Th atoms involved in $[ThF_7]^{3-}$, $[ThF_8]^{4-}$, and $[ThF_9]^{5-}$ monomers, dimers, trimers, tetramers and "polymers" (i.e. all clusters with a nuclearity equal to 5 or higher) at T = 1121 K in the LiF-ThF_4 system.

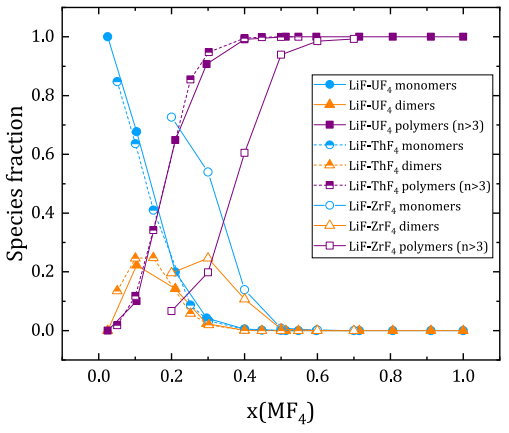

Fig. 5. Fraction of M atoms (M = Zr, Th, U) involved in monomers, dimers and polymers (i.e. trimers plus all clusters with a nuclearity equal to 4 or higher) at T = 1121 K in the LiF-ZrF_4 [63], LiF-ThF_4 (this work) and LiF-UF_4 [60] systems.

3.2.6. Trend as a function of the valence state of the actinide cation

No data seem to be available to this date on mixtures with UF_3. Thus the trends can only be discussed for the chloride systems, more specifically for NaCl-UCl_4 versus NaCl-UCl_3 systems. The 6-fold coordinated complex is dominant in the NaCl-UCl_4 mixtures above 32% UCl_4, while 7-fold and 8-fold coordinated complexes are also present in NaCl-UCl_3 mixtures above 25% UCl_3 [44,62]. This is in accordance with the trends already pointed out for the UCl_4 and UCl_3 end-members. The other major difference is the stability

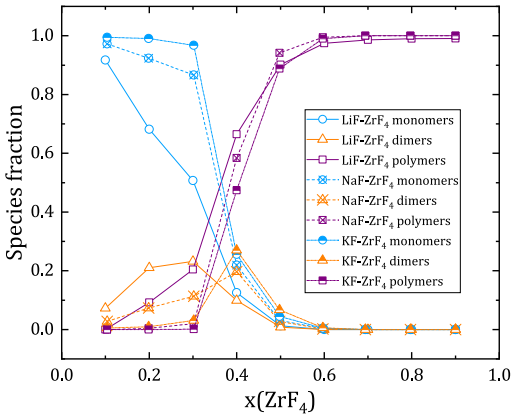

Fig. 6. Fraction of Zr atoms involved in monomers, dimers and polymers (i.e. trimers plus all clusters with a nuclearity equal to 4 or higher) at T = 1300 K in the LiF-ZrF_4 [63], NaF-ZrF_4 [54] and KF-ZrF_4 [54] systems.

of the solvation shells around U. The authors report a faster exchange of Cl^- ions in the first coordination shell around U^{3+} compared to U^{4+}, which translates to more stable clusters in NaCl-UCl_4 compared to NaCl-UCl_3. As for the network formation in both systems, bridging between isolated complexes by Cl^- ions is observed as soon as the concentration of uranium chloride in the mixture is sufficient. Oligomers with nuclearity higher than 4 become dominant (more than 50%) when $x(UCl_3)$ and $x(UCl_4)$ reach 0.3 and 0.4 M fractions, respectively [44]. This indicates that network formation is thus more favourable for the lower valence states.

3.3. Ternary actinide halide mixtures

A limited number of ternary mixtures with actinide halides have been investigated to this date, either experimentally or with computational methods. This report covers the results reported on some of the envisaged ternary fuel salt, coolant compositions or mixtures for pyrochemical processing applications, namely LiCl–KCl-UCl_3, LiF-ThF_4-UF_4, LiF-ThF_4-BeF_2, LiF-ZrF_4-BeF_2, NaCl-KCl-$MgCl_2$, NaCl-UCl_3-$MgCl_2$, and NaCl-UCl_4-$MgCl_2$. As detailed below the situation becomes even more intricate with respect to local structural properties when considering ternary mixtures.

3.3.1. Actinide plus two alkali halide solution: case study LiCl–KCl-UCl_3

Ternary mixtures in the LiCl–KCl-UCl_3 system, which are particularly relevant for pyrochemical processing applications, were investigated by Okamoto et al. [64], Li et al. [65], Song et al. [66], and Dai et al. [67] using EXAFS and atomistic simulations as listed in Table 5. $[UCl_6]^{3-}$ and $[UCl_7]^{4-}$ are the major complexes formed at low UCl_3 content, and $[UCl_7]^{4-}$/$[UCl_8]^{5-}$ at high UCl_3 concentra-

Table 5
Overview of the investigated ternary fluoride and chloride mixtures by various experimental and computational techniques. "CN(M)" indicates the coordination number around the central atom "M".

System	Mole fractions	T(K)	CN(M)	Technique	Ref.
LiCl–KCl-UCl_3 solutions					
LiCl–KCl-UCl_3	eutectic (5% UCl_3)	823	6.6/6.8(U)	EXAFS/PIM	[64]
LiCl–KCl-UCl_3	eutectic (17% UCl_3)	823	6.9/7.2(U)	EXAFS/PIM	[64]
LiCl–KCl-UCl_3	eutectic (50% UCl_3)	823	7.6(U)	PIM	[64]
LiCl–KCl-UCl_3	0.576–0.394–0.030	858.4/886/920.5/969.8/1019.4	6.35/6.26/6.17/6.22/6.13(U)	AIMD	[65]
LiCl–KCl-UCl_3	0.594–0.406–0.031	858/886/921/960/1019	6.35/6.26/6.17/6.22/6.13(U)	AIMD	[66]
LiCl–KCl-UCl_3	0.574–0.4–0.026	1023	6.3(U)	PIM	[67]
LiCl–KCl-UCl_3	0.559–0.389–0.052	1023	6.1(U)	PIM	[67]
LiCl–KCl-UCl_3	0.54–0.36–0.1	1023	6.6(U)	PIM	[67]
LiCl–KCl-UCl_3	0.472–0.328–0.2	1023	6.7(U)	PIM	[67]
LiF-ThF_4-UF_4 solutions					
LiF-ThF_4-UF_4	0.775–0.225–0.01	973	8.05(Th)/7.84(U)[a]	EXAFS/PIM	[57]
LiF-ThF_4-UF_4	0.775–0.225–0.02	973	8.09(Th)/7.88(U)[a]	EXAFS/PIM	[57]
LiF-ThF_4-UF_4	0.775–0.225–0.03	973	8.04(Th)/7.90(U)[a]	EXAFS/PIM	[57]
LiF-ThF_4-UF_4	0.775–0.225–0.04	973	8.08(Th)/7.89(U)[a]	EXAFS/PIM	[57]
LiF–BeF_2-ThF_4 solutions					
LiF–BeF_2-ThF_4	0.85–0.10–0.05	1273	7.57(Th)	PIM	[42]
LiF–BeF_2-ThF_4	0.636–0.314–0.05	1273	7.69(Th)	PIM	[42]
LiF–BeF_2-ZrF_4	0.85–0.10–0.05	1273	7.29(Th)	PIM	[42]
LiF–BeF_2-ZrF_4	0.636–0.314–0.05	1273	7.15(Th)	PIM	[42]
NaCl-KCl-$MgCl_2$ solutions					
NaCl-KCl-$MgCl_2$	eutectic	823	4.60(Mg)	AIMD	[68]
NaCl-UCl_3-$MgCl_2$ solutions					
NaCl-UCl_3-$MgCl_2$	0.4–0.4–0.2	1200	4.8(Mg), 6.7(U)	AIMD	[61]
NaCl-UCl_3-$MgCl_2$	0.333–0.333–0.333	1200	4.8(Mg), 6.7(U)	AIMD	[61]
NaCl-UCl_3-$MgCl_2$	0.25–0.25–0.5	1200	4.7(Mg), 6.7(U)	AIMD	[61]
NaCl-UCl_4-$MgCl_2$ solutions					
NaCl-UCl_4-$MgCl_2$	0.4–0.4–0.2	1200	4.4(Mg), 6.1(U)	AIMD	[61]
NaCl-UCl_4-$MgCl_2$	0.333–0.333–0.333	1200	4.5(Mg), 6.2(U)	AIMD	[61]
NaCl-UCl_4-$MgCl_2$	0.25–0.25–0.5	1200	4.5(Mg), 6.2(U)	AIMD	[61]

[a] MD data using the PIM.

tion. Isolated complexes are dominant below 20% UCl_3 and the network is sparse, as can be expected in a mixture with two alkali metal cations: the pattern is similar to that of binary mixtures of actinide halides with an alkali-metal halide.

3.3.2. Two actinide plus one alkali halide solution: case study LiF-ThF_4-UF_4

Bessada et al. investigated by coupled EXAFS/MD techniques LiF-ThF_4 eutectic mixtures ($x(LiF)$ = 0.775; $x(ThF_4)$ = 0.225) to which 1–4% of UF_4 was added [57]. The coordination environment of thorium (in particular coordination number) was affected very little by the UF_4 addition at those concentrations. However, a more pronounced impact was seen on the chemical speciation with 4% UF_4: namely, the fraction of thorium monomers $[ThF_n]^{4-n}$ and polymeric species $[Th_mF_n]^{4m-n}$ (dimers, trimers, etc.) decreased in favour of the formation of mixed clusters $[Th_mU_uF_n]^{4\ m+4u-n}$ and isolated $[UF_n]^{4-n}$ complexes (n = 6, 7, 8). This also lead to a slight increase in the fraction of free fluoride F^- anions as uranium disrupted the thorium network to form mixed uranium–thorium polymeric units $[Th_mU_uF_n]^{4\ m+4u-n}$, until a plateau was reached at 2% UF_4. This behaviour leads to a corresponding increase in the basicity of the salt, and a concomitant slight decrease in the viscosity as UF_4 is added [57].

3.3.3. The particular case of BeF_2 containing solutions: case study LiF–BeF_2-MF_4 (M = Th, Zr)

Beryllium fluoride is a strongly polymeric liquid, with a structure similar to that of silicate melts. BeF_2(cr) itself is a structural analogue to SiO_2(cr): the beryllium cations form a three-dimensional network of corner-sharing tetrahedra. This tetrahedral coordination is kept upon melting. In the LiF–BeF_2 melt, the melt shows mostly dissociated Li^+, BeF_4^{2-} and F^- species at low BeF_2 content. As the concentration of BeF_2 increases, dimers $Be_2F_7^{3-}$, trimers $Be_3F_{10}^{4-}$, tetramers $Be_4F_{13}^{5-}$, and higher degree polymers form progressively, until a completely connected network is obtained for pure BeF_2 [20,16,15].

Dai et al. investigated the structure of ternary LiF–BeF_2-ZrF_4 and LiF–BeF_2-ThF_4 melts using molecular dynamics simulations and PIM potentials [42]. The authors showed that for relatively low contents of BeF_2 (between 10 and 31.4%) and low contents of ThF_4/ZrF_4 (5%), Be^{2+} and Th^{4+} (resp. Zr^{4+}) retained a similar coordination environment to that observed in binary mixtures with LiF, i.e. isolated 4-fold coordinated complexes for Be^{2+} and mostly 7- and 8-coordinated Th^{4+} and Zr^{4+} cations in discrete units. Compared to pure LiF-ThF_4, however, the Th-Th RDFs in LiF–BeF_2-ThF_4 suggested a more compact structure with thorium complexes closer to each other. This can be related to the smaller ionic radius of Be^{2+} (0.27 Å) compared to Li^+ (0.76 Å). Moreover, the number of Th-F-Th bridging was found to increase, which is again a consequence of the smaller ionic radius, but also the higher charge of Be^{2+} compared to Li^+, and higher acidity [42]. Be^{2+} is expected to disrupt the Th-F-Th cross-linking less efficiently than Li^+: thus the network becomes more compact when adding Be^{2+} and sparser when adding Li^+. Dai et al. also performed a very instructive comparison with the structure properties in LiF–BeF_2-ZrF_4 melt. Generally, a lower coordination number is observed around Zr^{4+} compared to Th^{4+}, which can be understood from the lower ionic radius able to accommodate less F^- anions. Nevertheless this does not mean that the Zr complexes are less stable. On the contrary, calculations of the cage-out correlation times and energy activation barriers to escape the solvation shell indicate stronger Zr-F bonds and a more stable network in the ZrF_4 containing salt compared to the ThF_4 containing salt.

3.3.4. The particular case of $MgCl_2$ containing solutions: case study NaCl-KCl-$MgCl_2$ and NaCl-UCl_n-$MgCl_2$ (n = 3,4)

The addition of $MgCl_2$ to fuel salt mixtures is considered by some MSR designers to tailor the melting temperature of the fuel

to their needs [13], or as component of the coolant system. In this section, the features of the NaCl-KCl-$MgCl_2$ mixture are described, as they provide some first elements to predict the behaviour when $MgCl_2$ is added to the salt mixture. The local structure of pure $MgCl_2$ was scrutinized first by Raman spectroscopy, which revealed tetrahedral $MgCl_4^{2-}$ units in equilibrium with oligomers/polymers [69,70]. Neutron diffraction studies also later suggested a tetrahedral environment [71]. More recently, computational studies by reverse Monte Carlo techniques [72] and AIMD [73] indicated rather the predominance of 4-fold and 5-fold coordinated Mg^{2+} cations in equilibrium with 6-fold complexes, and a local symmetry closer to an octahedron with anion vacancies than a tetrahedron. The average Mg-Cl coordination number was calculated as 4.59 at 1000 K [73]. Temperature was found to have little influence on the coordination environment.

In the NaCl-$MgCl_2$ binary eutectic mixture, the coordination of Mg^{2+} cations was calculated to be 4.68 at 861 K by AIMD [74], corresponding to a distribution of CNs equal to 47.3%, 41.2% and 11.4% for the 5-fold, 4-fold and 6-fold coordinations, respectively [74]. In KCl-$MgCl_2$, a similar result was obtained by AIMD [75], where the local geometry was reported to evolve from predominantly (isolated) tetrahedral at low $MgCl_2$ content to distorted octahedral with one-two anion vacancies at high $MgCl_2$ content as network formation takes place, with an average coordination number varying between 4.22 (22.2% $MgCl_2$) and 4.78 (80% $MgCl_2$) at 1073 K. As pointed by the authors, the addition of $MgCl_2$ to a mixture will hinder the formation of isolated monomeric complexes, and in the contrary will result in network formation via chains of Mg^{2+} bridged by Cl^- anions. This will have an impact on the excesss thermodynamic properties as detailed in the next section, but also on transport properties, more particularly viscosity.

In the ternary NaCl-KCl-$MgCl_2$ eutectic mixture, the local structure is similar to that in the binaries with an average coordination number for Mg-Cl equal to 4.60 at 823 K, and the formation of corner-sharing and edge-sharing Mg chains of more than 9–10 units [68]. Li et al. [61] very recently reported AIMD simulations of NaCl-UCl_3-$MgCl_2$ and NaCl-UCl_4-$MgCl_2$ mixtures, that allow to scrutinize the effect of the Mg^{2+}addition on the network formation in actinide bearing salts, but also the difference in behaviour for a trivalent and tetravalent chloride salt mixture. Upon increasing concentration of $MgCl_2$, the network of $[U_mCl_n]^{3\ m-n}$ (resp. $[U_mCl_n]^{4\ m-n}$) polymers breaks down in both cases, but the effect is much greater in the UCl_4 salt mixture. About one third of the $[U_mCl_n]^{3\ m-n}$ polymers break down in the UCl_3 salt and are replaced by monomers, dimers, trimers and tetramers upon addition of $MgCl_2$, while the fraction of $[U_mCl_n]^{2\ m-n}$ oligomers and polymers grows simultaneously. In the UCl_4 salt, only 40% of the $[U_mCl_n]^{4\ m-n}$ polymer network remains, even at low $MgCl_2$ content, while only monomers and dimers are still present at high $MgCl_2$ content. Likewise, the fraction of $[Mg_mCl_n]^{2\ m-n}$ polymers increases in parallel. The average coordination number around U increases from 6.5 in NaCl-UCl_3 to 6.7 in NaCl-UCl_3-$MgCl_2$, while it increases from 6.1 in NaCl-UCl_4 to 6.2 in NaCl-UCl_4-$MgCl_2$ at 1200 K. As for the coordination around Mg, it is found around 4.7–4.8 in NaCl-UCl_3-$MgCl_2$, and around 4.4–4.5 in NaCl-UCl_4-$MgCl_2$ depending on the Mg content. Calculations of the free-energy barriers for the Cl^- anions to escape a coordination shell show that these are equivalent for Cl^- to escape the shell around Mg^{2+} and U^{3+}, while it takes more energy to escape the shell around U^{4+} compared to Mg^{2+}. This is related to the stronger U^{4+}-Cl^- bonds, as already detailed in Section 3.2.6, and explains the lower coordination numbers around Mg in the tetravalent uranium salt, but also the preferential formation of isolated complexes around U^{4+} when $MgCl_2$ is added, thus the easier disruption of the network structure.

3.4. Concluding note on the structural properties in the liquid

As a conclusion to this discussion on detailed features and general trends in structural properties of actinide bearing salts, it should be pointed out that most of the results obtained are based on atomistic simulations, which are challenging for actinide 5*f* element systems, and would thus require further validation with complementary experimental campaigns. Nevertheless, the overall picture provided with classical molecular dynamics, ab initio molecular dynamics, density functional theory, and machine-learning potentials studies is rather consistent and in line with the available experimental information, which gives confidence that the computed results reflect with good predictive capabilities the trends in these molten salt systems.

4. Thermochemical and thermophysical properties of actinide salt systems

4.1. Trends in stability of the actinide halides

Some selected thermodynamic properties, namely melting temperatures, enthalpies of fusion, entropies of fusion, sublimation entalpies, and heat capacity in the liquid phase are listed in Table 6 for the actinide trihalides and tetrahalides. The trends in the melting temperatures and sublimation enthalpies, displayed in Fig. 7, show a decrease in stability along the series of the actinides trihalides and tetrahalides (from Th to Am). The melting temperature and sublimation enthalpies are measures of the cohesion energy in the crystalline lattice. A similar decrease is also observed in other classes of materials, among the actinide oxides for instance [76]. As reported in [76], this indicates a predominant role of the 5*f* valence electrons on the bonding properties of the actinide compounds. When comparing to Fig. 1, it appears that the fluorides that display shorter An-X distances compared to the chlorides, also have a higher melting temperature and sublimation enthalpy. This is to be expected, as the fusion and sublimation events will require more energy when the bonding in the crystal lattice is stronger. Only the sublimation enthalpy of AmF_3 deviates from this trend, and we suggest re-assessing the latter data.

4.2. Mixing enthalpy data

The local structural properties as described in Section 3 can be related to excess thermodynamic properties as mentioned in the introduction, and in particular to the so-called mixing enthalpy data or excess enthalpy of mixing. The latter data is key when it comes to modelling the thermodynamic properties of salt systems using the CALPHAD method as described in Section 5.1. The Gibbs energy of mixing $\Delta_{mix}G_m$ is defined as the difference between the Gibbs energy of a solution before and after a mixing event between two end-members:

$$\Delta_{mix}G_m = \sum_i x_i\left(\overline{G_{m,i}} - G_{m,i}\right) \quad (4)$$

where $\sum_i x_i G_{m,i}$ is the initial Gibbs energy equal to the stoichiometric sum of the pure end-members, and $\sum_i x_i\overline{G_{m,i}}$ is the final Gibbs energy of the solution equal to the sum of partial molar Gibbs energies of components *i*.

The Gibbs energy of mixing is composed of an enthalpic and entropic component, $\Delta_{mix}H_m$ and $\Delta_{mix}S_m$, respectively, with a similar definition. In the case of an ideal solution, the entropy of mixing is given by:

$$\Delta_{mix}S_m^{ideal} = -R\sum_i x_i ln x_i \quad (5)$$

Table 6
Thermodynamic data on the most stable actinide fluorides and chlorides. Unless otherwise specified, the data were taken from the review by Capelli and Konings [6]. The data in italic are estimated.

Compound	T_{fus}(K)	$\Delta_{fus}H^{o}_{m}(T_{fus})$ (kJ·mol^{-1})	$\Delta_{fus}S^{o}_{m}(T_{fus})$ (J·K^{-1}·mol^{-1})	$\Delta_{sub}H^{o}_{m}(298.15K)$ (kJ·mol^{-1})	$C_p(l)$ (J·K^{-1}·mol^{-1})
Tetravalent actinide fluorides					
ThF_4	1383 ± 3	36.4 ± 10 [77]	26.3	349.7 ± 12.0[a]	168 ± 10 [77]
UF_4	1309 ± 5 [78]	44.79 [78]	34.2 [78]		174.74 [78]
Tetravalent actinide chlorides					
$ThCl_4$	1042 ± 2	61.5 ± 2.6	59.0	234.9 ± 5.4[a]	*167.4 ± 10*
UCl_4	863 ± 1	45 ± 8	52.1	203.4 ± 5.3[a]	108 + 0.06T
Trivalent actinide fluorides					
UF_3	1768 [79]	36.8 [79]	20.8 [79]		130 [79]
NpF_3	*1735 ± 30*	*36.1 ± 5*	*20.8*	417 ± 21.7[a]	*132 ± 20*
PuF_3	1705 ± 10	35.4 ± 5	20.8	418.9 ± 5.2[a]	*130 ± 20*
AmF_3	1666 ± 20	*34.7 ± 5*	20.8	437.5 ± 21.7[a]	*130*
Trivalent actinide chlorides					
UCl_3	1115 ± 2	49 ± 2	43.9	340.7 ± 20.1[a]	*129.7*
$NpCl_3$	1070 ± 3	50 ± 8	46.7	*307.8 ± 10.8*[a]	*137.5 ± 15*
$PuCl_3$	1041 ± 2	49 ± 3	47.1	312.2 ± 2.7[a]	*144*
$AmCl_3$	991 ± 5	48.1 ± 4			*146.2 ± 6*

[a] Uncertainty recalculated in this review.

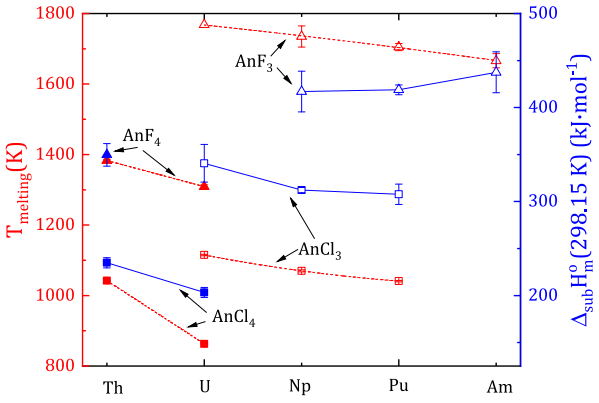

Fig. 7. Evolution of the melting temperature (in red) and sublimation enthalpy (in blue) along the series of the actinide halides.

and the enthalpy of mixing is equal to zero, which means the solution is stabilized by the entropy term only, called the configurational entropy.

Most systems deviate from ideal behaviour, however, and the excess molar Gibbs energy of mixing $\Delta_{mix}G^{excess}_{m}$ quantifies their deviation from ideality:

$$\Delta_{mix}G^{excess}_{m} = \Delta_{mix}G_{m} - \Delta_{mix}G^{ideal}_{m} \quad (6)$$

$$\Delta_{mix}G^{excess}_{m} = \Delta_{mix}H^{excess}_{m} - T\Delta_{mix}S^{excess}_{m} \quad (7)$$

where $\Delta_{mix}H^{excess}_{m}$ and $\Delta_{mix}S^{excess}_{m}$ are the excess enthalpy and entropy of mixing, respectively, given by:

$$\Delta_{mix}S^{excess}_{m} = \Delta_{mix}S_{m} + R\sum_{i} x_i ln x_i$$
$$\Delta_{mix}H^{excess}_{m} = \Delta_{mix}H_{m} \quad (8)$$

Since the ideal enthalpy of mixing is equal to zero, the excess enthalpy of mixing is given directly by the measured enthalpy of mixing data.

Various techniques have been reported to collect such data using calvet-type twin microcalorimetry, among which "drop", "indirect drop", "break-off bubble", "break-off ampoule", "suspended cup" methods [80,81] and conventional differential scanning calorimetry [82]. A vary large databank has been collected on binary mixtures of halides salts, mainly by Kleppa, Papatheodorou, Gaune-Escard, Hattem and co-workers as cited below in the 1960s-to this date, which have contributed to the understanding of the relationship between this excess thermodynamic property and local structure behaviour. At the time of the measurements, the structural information available came mostly from Raman studies. It is very informative to re-interpret those data in light of the more recent information collected using techniques such as in situ EXAFS, neutron diffraction, first-principles and classical molecular dynamics simulations. This review focuses on the fuel salt systems mentioned in the previous sections, and for which the structural properties have been discussed more at length.

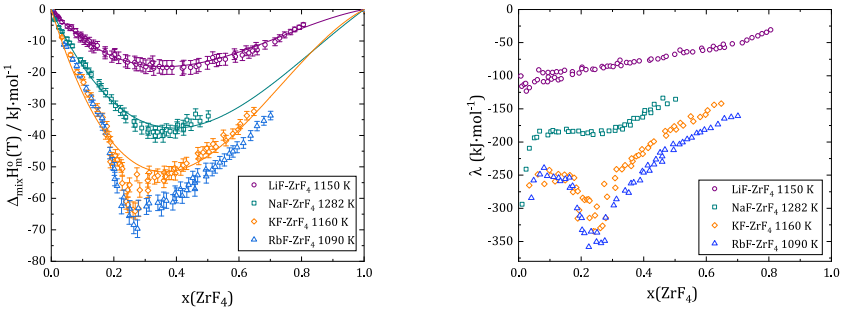

(a) $\Delta_{mix}H^{o}_{m}$ (b) λ

Fig. 8. (a) Enthalpies of mixing and (b) interaction parameters for the LiF-ZrF_4, NaF-ZrF_4, KF-ZrF_4 and RbF-ZrF_4 systems measured by Hattem et al. [88]. The lines are polynomial fits to the data.

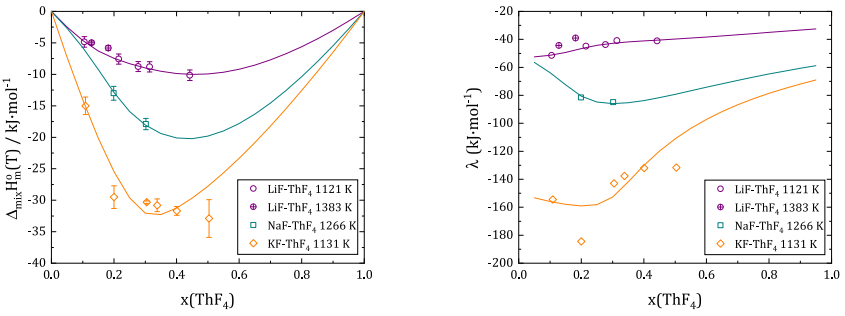

(a) $\Delta_{mix}H^{o}_{m}$ (b) λ

Fig. 9. (a) Enthalpies of mixing and (b) interaction parameters for the LiF-ThF$_4$, NaF-ThF$_4$, and KF-ThF$_4$ systems measured by Capelli et al. [82], Schreuder et al. [89] and Ocadiz et al. [90]. Comparison with the thermodynamic models (solid lines) of Ocadiz et al. [91] (LiF-ThF$_4$), and Ocadiz et al. (NaF-ThF$_4$ and KF-ThF$_4$) [90].

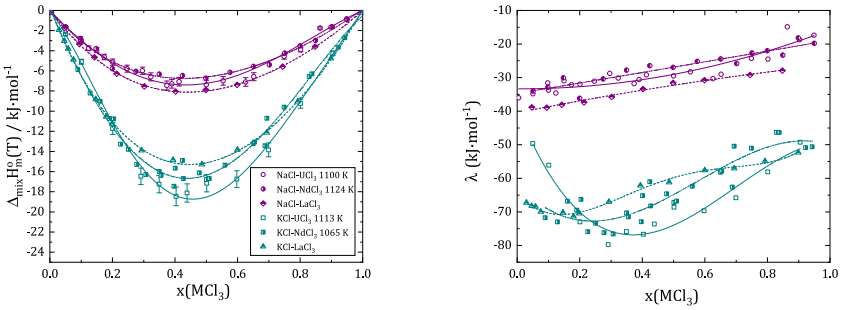

(a) $\Delta_{mix}H^{o}_{m}$ (b) λ

Fig. 10. (a) Enthalpies of mixing and (b) interaction parameters for the NaCl-UCl$_3$ [85], KCl-UCl$_3$ [84], NaCl-NdCl$_3$ [92], KCl-NdCl$_3$ [92], NaCl-LaCl$_3$ [83] and KCl-LaCl$_3$ [83] systems. The lines are polynomial fits to the data.

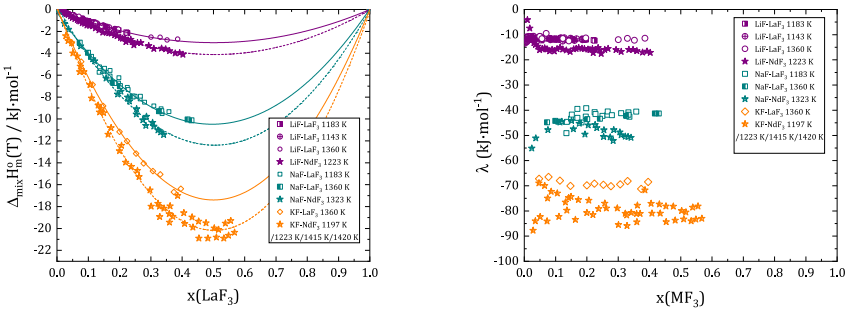

(a) $\Delta_{mix}H^{o}_{m}$ (b) λ

Fig. 11. (a) Enthalpies of mixing and (b) interaction parameters for the LiF-LaF$_3$ [93,94], NaF-LaF$_3$ [93,94], KF-LaF$_3$ [93], LiF-NdF$_3$ [95], NaF-NdF$_3$ [95] and KF-NdF$_3$ [95] systems. The lines are polynomial fits to the data.

Some general trends can be pointed out. Firstly, the enthalpy of mixing in most binary molten salt fluoride and chloride systems is negative (although not always), indicating an exothermic process. The enthalpy of mixing is the result of coulombic interactions, dispersion interactions, as well as ordering effects (complexing and network structure formation) in the mixture [83]. In a binary mixture of an alkali metal or alkaline-earth halide with a trivalent or tetravalent halide (e.g. ZrF$_4$, ThF$_4$, UCl$_3$, LaF$_3$, LaCl$_3$ etc.), the mixing enthalpy increases in absolute value along the series as the ionic radius of the alkali metal or alkaline-earth metal increases. This is seen in Figs. 8–12, displaying the mixing enthalpy data of AF-ZrF$_4$, AF-ThF$_4$, ACl-UCl$_3$, AF-LaF$_3$, AF-NdF$_3$, and ACl-MgCl$_2$ mixtures (A = Li, Na, K, Rb, Cs). According to theory developed by Hong and Kleppa [84], the value of the mixing enthalpy of a mixture with cations in different valence states (so called charge-unsymmetrical or asymmetrical mixed cations with common anion) can be related to the "relative ionic potential" of the cations given by the formula:

$$\Delta IP = z_1/r_1 - z_2/r_2 \tag{9}$$

where z_1, z_2, r_1 and r_2 correspond to the oxidation state and ionic radii of the cations 1 and 2, respectively. From the above formula, one sees that the "relative ionic potential" increases when the size of the alkali metal cation increases, which causes an increase in the absolute value of the mixing enthalpy. Moreover, systems with the same charge and similar ionic radii will display very similar enthalpies of mixing. This is the case for instance for NaCl-UCl$_3$ [85] and KCl-UCl$_3$ [84], which are very close in magnitude to the analogue systems NaCl-NdCl$_3$, NaCl-LaCl$_3$ and KCl-NdCl$_3$, KCl-LaCl$_3$, respectively (see Fig. 10).

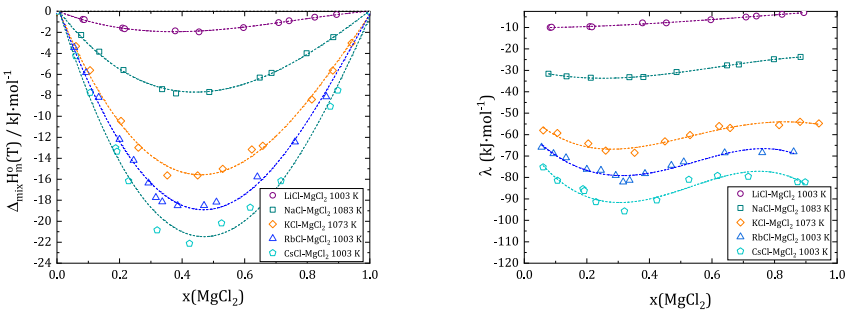

Fig. 12. (a) Enthalpies of mixing and (b) interaction parameters for the ACl-$MgCl_2$ (A = Li, Na, K, Rb, Cs) systems measured by Kleppa and McCarty [87]. The lines are polynomial fits to the data.

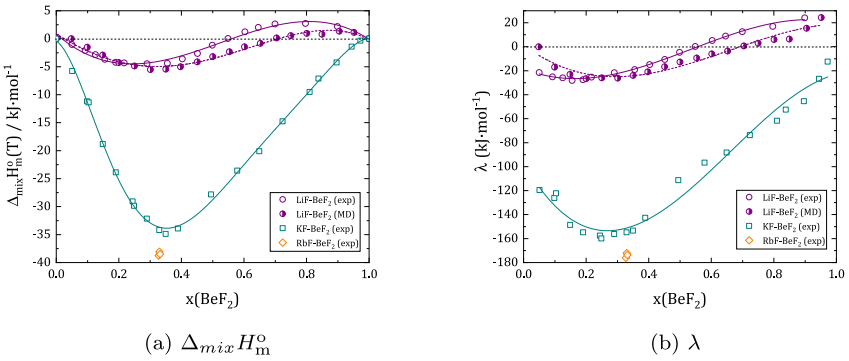

Fig. 13. (a) Enthalpies of mixing and (b) interaction parameters for the LiF–BeF_2, KF-BeF_2, and RbF-BeF_2 measured by Holm and Kleppa [96]. For LiF–BeF_2, a comparison is also made with the data derived from MD simulations [20]. The lines are polynomial fits to the data.

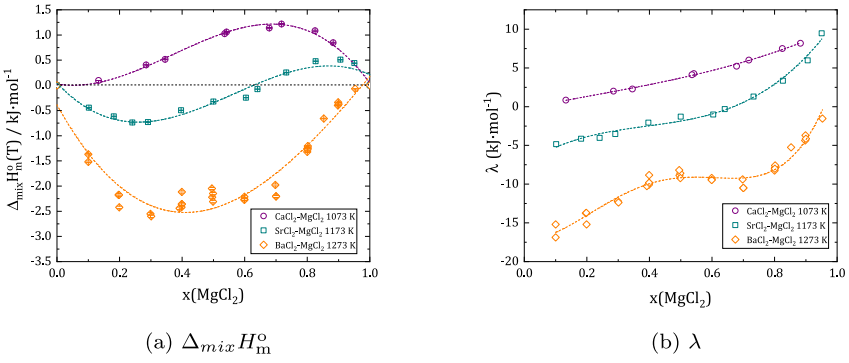

Fig. 14. (a) Enthalpies of mixing and (b) interaction parameters for the AECl-$MgCl_2$ (AE = Ca, Sr, Ba) systems measured by Papatheodorou and Kleppa [97]. The lines are polynomial fits to the data.

The energetic asymmetry of the binary system A_nX_m-B_uX_v system can be quantified using the interaction parameter λ:

$$\lambda = \Delta_{mix}H_m/(x(B_uX_v)\cdot(1-x(B_uX_v))) \quad (10)$$

where $\Delta_{mix}H_m$ is the measured mixing enthalpy and $x(B_uX_v)$ the molar fraction in B_uX_v.

The evolution of the interaction parameters for the systems considered is shown along with the mixing enthalpy data in Figs. 8–14. One sees again that the magnitude of the interaction parameter increases towards more negative values with increasing size the alkali/alkaline-earth cation [83]. Moreover, more negative values are obtained in alkaline/alkaline-earth rich regions compared to the trivalent/tetravalent halide rich regions, indicating asymmetric systems from the energetics point of view.

The position of the minima in the mixing enthalpy and interaction parameter data are strongly linked to the local structure properties and more specifically to the formation of molecular species and network formation. For binary mixtures of the type AX-MX_2 with divalent cations, a minimum in the interaction parameter is observed around 0.33% due to the formation of MX_4^{2-} complexes [86]. This is the case in the ACl-$MgCl_2$ (A = Li, Na, K, Cs, Rb) mixtures for instance [87] (Fig. 12). In a number of binary mixtures with trivalent cations of the type AX-MX_3, the minimum is shifted towards higher compositions around 0.4% pointing to the formation of MX_6^{3-} complexes [86,84]. This is especially visible for KCl-UCl_3 presented here in Fig. 10. For the tetravalent cations shown here (Zr, Th and U), the minimum is also around 33% for the ZrF_4 systems due to the high stability of ZrF_6^{2-} complexes, and shifted

towards slightly higher values in the ThF_4 solutions ($\sim$ 0.4–0.5%), in relation with the higher coordination numbers observed in the corresponding melts. The minimum becomes more evident when the size of the alkali cation increases, which can be related to the more stable isolated complexes as detailed in the previous section.

The comparison of the data for LiF-ZrF_4 (Fig. 8) and LiF-ThF_4 (Fig. 9) allows to study the influence of the ionic radius of the tetravalent cation. A more negative mixing enthalpy is observed in the ZrF_4 melt, which is due to the shorter and stronger Zr-F bonds, more stable $[ZrF_n]^{4-n}$ complexes and reduced tendency to form a network by Zr-F-Zr cross-linking [60].

BeF_2 and $MgCl_2$ containing salts present particularly interesting features, with in some cases the appearance of a S-shaped mixing enthalpy curve. This is the case for LiF–BeF_2 (Fig. 13), with positive mixing enthalpy data (endothermic contribution) at high BeF_2 content, and negative values (exothermic contribution) at high LiF content. This occurrence of this S-type behaviour was explained by the disruption of the highly connected three-dimensional polymeric structure of liquid BeF_2 upon addition of LiF. The breakdown of Be-F-Be bridges causes this positive contribution to the mixing enthalpy [96,20]. This pattern is very well captured by the MD simulations using PIM parameters (see Fig. 13), although the magnitude is slightly overestimated [20]. Moreover, the minimum of the curve occurs around $x(BeF_2)\sim$0.3–0.4, which indicates the stability of BeF_4^{2-} complexes. Interestingly, this S-shape disappears when a larger alkali metal is added to BeF_2: KF-BeF_2 and RbF-BeF_2 show the typical exothermic behaviour over the full composition range. Because of the larger ionic radii of K^+ and Rb^+, we can expect a decreased tendency towards polymerization and an increased stabilisation of the isolated BeF_4^{2-} complexes.

Finally, the binary mixtures of $MgCl_2$ with alkaline-earth Ca, Sr and Ba chlorides offer a very interesting case study. As shown in Fig. 12, the results obtained for $CaCl_2$-$MgCl_2$ are endothermic with a maximum at 0.7% $MgCl_2$ around 1.2 kJ·mol^{-1}, while the data for $BaCl_2$-$MgCl_2$ show exothermic behaviour with a minimum at 0.4% $MgCl_2$ around $-$2.5 kJ·mol^{-1}. $SrCl_2$-$MgCl_2$ is intermediate in behaviour and presents a S-shape similar to the one observed in the LiF–BeF_2 system (although less marked), which must be related to the tendency that $MgCl_2$ presents towards polymerization [97]. The Mg-Cl bond thus shows a covalent character leading to the formation of Mg-Cl-Mg bridges [97]. As reported by Papatheodorou and Kleppa, breaking the bridges leads to a significant endothermic contribution to the enthalpy of mixing, that dominates over the coulombic and dispersion forces contributions [97]. But here again, the S-shape is not systematically observed, but rather limited to very specific situations: the mixtures with alkali metal chlorides or with $BaCl_2$ lead to the typical exothermic trend. Interestingly, an endothermic mixing enthalpy is obtained for $CaCl_2$-$MgCl_2$, while an exothermic one is reported for NaCl-$MgCl_2$, although Na^+ and Cs^{2+} have very similar ionic radii (1.02 Å and 1.0 Å in 6-fold coordination), respectively. This shows how complex the local structure properties and their relation to the excess properties can be.

As mentioned previously, mixing enthalpies are key input data when it comes to performing thermodynamic assessments of molten salt systems (see Section 5.1), but are not always available in the literature, and especially not for actinide bearing salts apart for the few systems listed here (i.e. LiF-ThF_4, NaF-ThF_4, KF-ThF_4, NaCl-UCl_3 and KCl-UCl_3). Some empirical estimation methods have been developed over the years for binary charge symmetrical and asymmetrical systems as a function of cation radii, including the conformal solution model of Reiss, Katz and Kleppa (RKK) [98], the modified conformal solution model by Davis and Rice [99] and Davis [100,101], a complex anion model by Flengas and Kucharski [102], and more recently the approach by Schorne-Pinto et al. [103] that builds on the method of Davis. We will not give a detailed description of the latter works as this is beyond the scope of this article, but will outline shortly the method of Davis that has been widely used and appears suitable for a number of systems, and the recent additions made by Schorne-Pinto et al. that were tested on akali metal chloride - rare-earths/uranium trichloride systems. To a first approximation in the conformal solution theory of Davis [100,101], the asymmetry parameter λ in a system AX-MX_n varies, at fixed temperature, pressure and composition, linearly with the size parameter δ_{12}. δ_{12} is a function of ionic radii and distances of ionic species $d_1 = (r_{A^+} + r_{X^-})$ and $d_2 = (r_{M^{n+}} + r_{X^-})$ and is defined as follows:

$$\delta_{12} = \frac{d_1 - d_2}{d_1 \cdot d_2} = \frac{(r_{A^+} + r_{X^-}) - (r_{M^{n+}} + r_{X^-})}{(r_{A^+} + r_{X^-}) \cdot (r_{M^{n+}} + r_{X^-})} \quad (11)$$

where $r_{A^+}, r_{M^{n+}}$, and r_{X^-} are the ionic radii of the alkali cation, M metal cation (e.g. alkaline-earth, rare-earth, actinide), and X anion, respectively, taken from the Shannon tabulated data [25] in sixfold coordination. Later works have shown that for series where the ionic radius of the metal cation varies widely, a quadratic fitting as a function of δ_{12} improves the description, however [104,103]. When using the approach of Davis, the minimum value for the mixing enthalpy is often assumed in the literature to be located at the equimolar composition, as pointed out by Schorne-Pinto et al., which is not correct for most charge asymmetrical systems, however. A more correct approach would consist in applying the method to every composition point, but this is very time consuming. Schorne-Pinto et al. [103] thus propose to first determine the composition of maximum short-range ordering before applying the analysis method of Davis with quadratic fitting to the mixing enthalpy data at the composition of maximum short range ordering (SRO). The authors show that for alkali metal-rare earth trichloride systems, the composition of maximum SRO follows a linear evolution with respect to δ_{12}. They demonstrate the reliability of the proposed methodology by estimating the mixing enthalpy of NaCl-UCl_3 and KCl-UCl_3 at this maximum SRO composition based on the data of sodium chloride-rare earth trichloride systems available in the literature. They subsequently apply the same method to make estimates of the mixing enthalpies for the other alkali metal-uranium chloride systems (i.e. Li, Rb and Cs-based melts), as well as for the ACl-$PuCl_3$ (A = Li, Na, K, Rb, Cs). Such input is very valuable considering the scarcity of data in plutonium-based systems. The methodology described above is applicable as long as sufficient information can be found to establish trends of the asymmetry parameter and maximum short range ordering (SRO) compositions as function of δ_{12} over a range of cation radii that is wide enough. This is the case for the trichloride salt systems, but probably not for the trifluorides where far less studies have been reported. It is also not directly suitable for estimating the mixing enthalpies of tetravalent actinide salt systems since only the cerium and zirconium surrogates are stable in the tetravalent state.

4.2.1. Density, molar volume and viscosity

The structural features of the halide salts can also be related to the evolution of other thermophysical properties such as density/-molar volume, thermal expansion or transport properties such as viscosity, thermal or electrical conductivity. The intent here is not to give an exhaustive review of the latter properties for each system, as this has been the subject of other works, notably by Beneš and Konings [5] and Capelli and Konings [6]. Instead, we will illustrate with a few examples the link between local structure and those properties in selected systems.

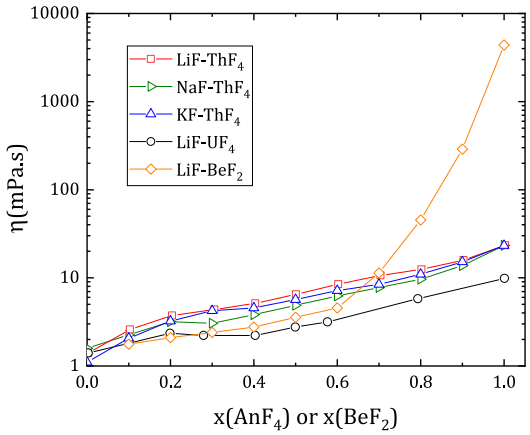

Fig. 15. Viscosity of LiF-ThF_4 [106], NaF-ThF_4 [107], KF-ThF_4 [107], LiF-UF_4 [108] salts at T = 1273 K, and that of LiF–BeF_2 [109] at T = 1200 K.

Starting with density, it is found that pure tetrafluorides melts (e.g. UF_4 and ThF_4) are denser than trichloride melts (e.g. UCl_3) [6], which can be directly related to the stronger and shorter An-X bonds (Fig. 1). Ideal behaviour is rather common in binary mixtures, for instance in LiF-ThF_4 and LiF-UF_4, meaning molar volumes of mixtures are obtained by simple stoichiometric sum of the end-members [91]. However, some of the systems show greater deviations from ideality, for instance NaCl-UCl_3, which was related to the increased covalency of the An-Cl bonds [91,105]. In the LiF–BeF_2 mixture, a S-shape is observed when plotting the excess molar volume versus composition, similar to that of the mixing enthalpy data with a minimum observed around $x(BeF_2) \sim 0.4$ and a positive deviation at high BeF_2 content [20]. The minimum in the density data corresponds to the composition region where the liquid transitions from molecular with mainly BeF_4^{2-} species to polymeric with appearance of dimers, trimers, etc. The positive deviation is again related to the breakdown of the three-dimensional network of BeF_2 upon addition of LiF [20].

Viscosity is also directly related to local structure properties. UF_4 and ThF_4 show again greater viscosity than UCl_3 [91], which is explained by the stronger An-X bonds and greater network forming capabilities. As illustrated in Fig. 15, a higher viscosity is observed in LiF-ThF_4 compared to NaF-ThF_4 and KF-ThF_4. This can be easily understood from the fact that the bigger the alkali cation is, the easier it can disrupt network formation and favour isolated complexes. The viscosity of LiF-UF_4 is also lower than that of LiF-ThF_4, indicating a "weaker" network structure in the uranium melt. Finally, the viscosity of the aforementioned binary actinide halide salts is still about 3 orders of magnitude lower than in LiF–BeF_2 at high BeF_2 content, which reflects the much greater degree of polymerization in the beryllium containing salt.

5. Modelling methods of the thermochemical and thermophysical properties of molten salts

The development of modelling methods of the thermochemical and thermophysical properties of molten salts is essential to assess the behaviour under any set of (temperature, pressure, redox potential etc.) conditions during normal operation and accidental conditions in a Molten Salt Reactor. Performing an exhaustive assessment through models and simulation codes of the dynamic and complex fuel physical-chemistry is a stringent requirement for the safety analysis and the licensing process. In recent years, the atomistic simulations (e.g. *ab initio* molecular dynamics, density functional theory, classical molecular dynamics) of the thermodynamic and transport properties have undergone a substantial development. However, they also have their own limitations, in particular they are computationally expensive and cannot give direct information on the equilibrium thermodynamics, which makes them impractical for use on multi-element systems in operating conditions. This review focuses rather on the modelling methods developed for thermodynamic (Section 5.1), density and viscosity (Section 5.2) properties at the mesoscale, based on the CALPHAD (CALculation of PHAse Diagram) methodology [110].

5.1. Thermodynamic modelling

The CALPHAD method is based on the least-square minimization of the total Gibbs energy of the system [110], and requires to express the Gibbs energy functions of all phases (solid, liquid, gas) in the system under consideration. Excess parameters in the Gibbs energy functions are optimized to fit as best as possible all the thermodynamic information available, including phase diagram data, thermodynamic functions (enthalpies of formation, standard entropies, heat capacities), vapour pressures, chemical potentials etc.

Various formalisms exist to model the solid, liquid and gaseous phases, and are selected depending on the nature of the system under consideration (e.g. metallic, oxide, salt system) to reflect as best as possible its intrinsic physico-chemical properties. We treat here exclusively the solution models reported for the liquid salt, which is the prime interest in this review. Two main formalisms are in use in the literature for halide salts, namely the associate model [110,111] and the quasi-chemical model proposed by Pelton et al. [112–115] in the quadruplet approximation. Both are particularly well-adapted for ionic liquids with strong short-range ordering as is the case for the halide salts.

In the former method, so-called associate species are defined in the liquid solution with a stoichiometry similar to that of crystalline phases that correspond to "stable" clusters in solution, i.e. with a significant lifetime compared to the mean time between thermal collisions [110]. Their Gibbs energies are optimized along with other thermodynamic excess parameters in the assessment. Examples of systems optimized with this formalism are LiF-NaF-KF-CrF_3 [116] or NaF-BeF_2 [117]. However, as pointed out by Pelton [118] and stressed again in the recent reviews of Besmann and Schorne-Pinto [119] and Sundman et al. [111], this description is not applicable for systems with positive deviations from ideality, and is not completely satisfactory when it comes to extrapolation to higher-order systems.

The latter method, i.e. the quasi-chemical model (QCM) in the quadruplet approximation [112–115], is the one retained for the large thermodynamic databases of salt systems for nuclear applications, in particular the Joint Research Centre Molten Salt Database (JRCMSD) in Europe [14], or the Molten Salt Thermal Properties Database-Thermochemical (MSTDB-TC) in the US [119,130]. The quasi-chemical formalism was first introduced by Guggenheim [120], and then adapted by Pelton and Blander [121] to allow more freedom in the optimization of the minima of the mixing enthalpy and entropy (i.e. not limited to the equimolar composition) [119]. The modified quasi-chemical model in the pair approximation was then developed further by Pelton et al. for binary solutions [112], by Pelton and Chartrand for multi-component solutions [113], by Chartrand and Pelton for two sublattices [114], and finally by Pelton et al. with the addition of the quadruplet approximation [115].

In the modified quasi-chemical model in the quadruplet approximation, the basic unit in the liquid solution is a quadruplet composed of two cations and two anions (this could be two different anions for a reciprocal solution, or a common anion). In the example shown below, one cation is noted A^+ (e.g. alkaline cation),

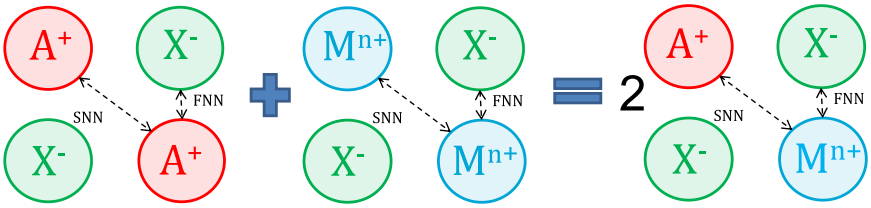

Fig. 16. Schematic representation of the second-nearest neighbour (SNN) exchange reaction of the quadruplets.

the other cation is noted M^{n+} (e.g. actinide cation), and the (common) anion is written X^- (Fig. 16). In the quadruplet, both first-nearest neighbour (FNN) and second-nearest neighbour (SNN) interactions between ions of opposite and same charge, respectively, are taken into account. The optimized excess Gibbs energy parameters are then related to the second-nearest neighbour (SNN) exchange reaction of the quadruplets as shown in Fig. 16.

The associated Gibbs energy change $\Delta g_{AM/X}$ is given by:

$$\Delta g_{AM/X} = \Delta g^{o}_{AM/X} + \sum_{i\geqslant 1} g^{i0}_{AM/X}\chi^{i}_{AM/X} + \sum_{j\geqslant 1} g^{0j}_{AM/X}\chi^{j}_{MA/X} \tag{12}$$

where $\Delta g^{o}_{AM/X}$ and $g^{ij}_{AM/X}$ are coefficients that are composition independent but may vary with temperature.

The composition dependence $\chi^{i}_{AM/X}$ is itself related to the cation-cation pair mole fractions X_{AA}, X_{MM}, and X_{AM} as follows:

$$\chi_{AM/X} = \frac{X_{AA}}{X_{AA} + X_{AM} + X_{MM}} \tag{13}$$

One of the major feature of this model is the ability to select, by varying the ratio between cation-cation coordination numbers Z^{A}_{AM/X_2} and Z^{M}_{AM/X_2} [4], the composition of maximum short range ordering where the total Gibbs energy has its minimum. The latter composition is related to the minimum in the mixing enthalpy curve and most often very close to the lowest eutectic in the phase diagram. To ensure conservation of charge, the anion-anion coordination number is subsequently given by:

$$\frac{q_A}{Z^{A}_{AM/X_2}} + \frac{q_M}{Z^{M}_{AM/X_2}} = \frac{q_X}{Z^{X}_{AM/X_2}} + \frac{q_X}{Z^{X}_{AM/X_2}} \tag{14}$$

One limitation of the formalism described above, however, is the fact that a single coordination number is selected and fixed for every cation (A and M) in the solution, regardless of the composition [119]. This of course does not reflect the real local structure of the salt melt, especially for cations with a charge higher than one, as we have seen in Section 3. Coordination numbers vary with composition, and the melt structure can evolve from a truly dissociated melt towards molecular species and oligomerization when the concentration of cations with valence >+2 are introduced at higher concentrations.

To provide a more physical description, Robelin and Chartrand proposed an extension of the QCM in the quadruplet approximation by introducing variable coordination numbers [122,123]. To this end, additional species are introduced on the cationic sub-lattice, and thus more end-member compounds are defined. In the case of the NaF-AlF_3-CaF_2-BeF_2 -Al_2O_3-BeO system considered by the authors [122,123], the cations considered were Na^+, Al^{3+}_V, Al^{3+}_{IV}, Al^{6+}_2, Ca^{2+}, Be^{2+}_{IV}, Be^{4+}_2, while the anions were F^- and O^{2-}, respectively. We shall focus our discussion on the NaF-BeF_2 sub-system, which is more in line with the focus of this article. The Be^{2+}_{IV} and Be^{4+}_2 cations correspond to the isolated BeF^{2-}_4 complex and the dimer species $Be_2F^{3-}_7$, respectively. Two compositions of maximum short-range ordering are subsequently defined. As pointed out in the recent review by Besmann and Schorne-Pinto, this methodology allowed to obtain a better agreement with the phase equilibrium data compared to the "traditional" approach [124] with fixed coordination numbers over the entire composition range.

[4] Note that we are here talking about cation-cation coordination numbers of A around M, and M around A, not of the cation–anion coordination numbers of X around A and X around M.

Table 7
Summary of species used on the cationic and anionic sublattices of QCMs in the quadruplet approximation with variable coordination numbers.

System	Species on the cationic sublattice	Species on the anionic sublattice	Ref.
NaF:BeF_2	Na^+, Be^{2+}_{IV}, Be^{4+}_2	F^-	[122,123]
LiF:BeF_2	Li^+, Be^{2+}_{IV}, Be^{4+}_2, Be^{6+}_3	F^-	[20]
LiF:UF_4	Li^+, U^{4+}_{VII}, U^{4+}_{VIII}, U^{8+}_2	F^-	[60]
NaF:ThF_4	Na^+, Th^{4+}_{VII}, Th^{4+}_{VIII}, Th^{8+}_2	F^-	[89]
NaCl:UCl_3	Na^+, U^{3+}_{VI}, U^{3+}_{VII}, U^{6+}_2	Cl^-	[49]
NaF:ZrF_4	Na^+, Zr^{4+}_{VI}, Zr^{4+}_{VII}, Zr^{8+}_2	F^-	[54]
KF:ZrF_4	K^+, Zr^{4+}_{VI}, Zr^{4+}_{VII}, Zr^{8+}_2	F^-	[54]

In a similar effort, Smith and co-workers have recently developed such models for the LiF–BeF_2 [20], LiF-UF_4 [60], NaF-ThF_4 [89], NaCl-UCl_3 [49], NaF-ZrF_4 and KF-ZrF_4 [54] systems. In each case, the choice of the species on the cationic sub-lattice was dictated by the chemical speciation data provided by EXAFS and MD simulations. In order to limit the number of fitting parameters from growing too large, a selection was made for the most prevalent species as detailed in Table 7. Note that in the LiF–BeF_2 system, the largest polymeric unit considered is the trimer $Be_3F^{4-}_{10}$, meaning that pure beryllium fluoride is modelled with a fully connected network of trimers. In the other systems, a dimer species (e.g. $U_2F^{6-}_{14}$, $Th_2F^{5-}_{13}$, $U_2Cl^{6-}_{12}$, $Zr_2F^{-}_{9}$, and $Zr_2F^{3-}_{11}$, respectively) represents the largest unit. This difference is meant to reflect the large difference in the degree of polymerization occurring between pure beryllium and actinide (or other transition metal) containing melts. Such difference is clearly visible when looking at a property such as viscosity (see Fig. 15). For more detail on the exact implementation of such coupled structural-thermodynamic models, the reader is referred to the corresponding papers. One notable feature in the latter works, finally, is the use of the output of molecular dynamics simulations on chemical speciation in the melt to optimize the excess Gibbs energy parameters. This is illustrated for the NaCl-UCl_3 system in Fig. 17 where the chemical speciation as calculated by MD is compared to that implemented in the CALPHAD model, together with the calculated phase equilibria points.

5.2. Density and viscosity modelling

Molar volume V_m and density ρ of the liquid solution, which are directly related to each other via $\rho = M/V_m$ (M being the molar mass), can also be modelled using a quasi-chemical formalism, by introducing temperature-dependent molar volume expressions for the pure end-members and pressure-dependent excess Gibbs

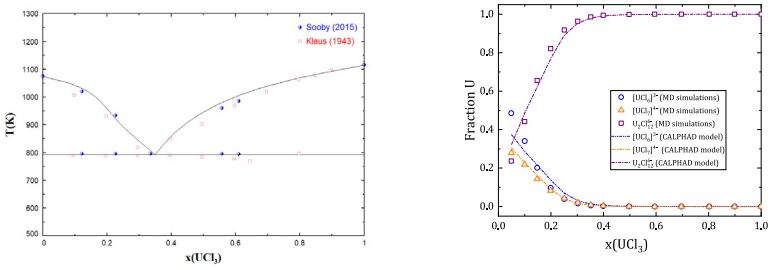

(a) Phase diagram (b) Speciation

Fig. 17. (a) Phase diagram of the NaCl-UCl_3 system and (b) chemical speciation at T = 1400 K as modelled by [49].

energy parameters for the mixtures as described in detail in [125]. The previous Gibbs energy expression (Eq. 12) then becomes:

$$\begin{aligned} \Delta g_{AM/X} = \Delta g^{0}_{AM/X} + \beta^{0}_{AM/X}(P-1) \\ +\sum_{i\geqslant 1}\left[g^{i0}_{AM/X} + \beta^{i0}_{AM/X}(P-1)\right]\chi^{i}_{AM/X} \\ +\sum_{j\geqslant 1}\left[g^{0j}_{AM/X} + \beta^{0j}_{AM/X}(P-1)\right]\chi^{j}_{AM/X} \end{aligned} \quad (15)$$

where P is the pressure, and $\beta^{0}_{AM/X}$, $\beta^{i0}_{AM/X}$ and $\beta^{0j}_{AM/X}$ are the pressure-dependent parameters being optimized in the density model, that are independent of composition, but can have a temperature dependence.

This method has been applied successfully to systems such as NaCl-KCl-$MgCl_2$-$CaCl_2$ [125], NaF-AlF_3-CaF_2-Al_2O_3 [122], as well as nuclear fuel systems LiF-ThF_4, LiF-UF_4, LiF-ThF_4-UF_4 and NaCl-UCl_3 [91].

Coupled thermodynamic-viscosity models have finally been reported in the literature based on an Eyring [126–128] equation (Eq. 16) whose molar activation energy for viscous flow G^{*} is expanded as a first-order polynomial in the quadruplet mole fractions (Eq. 17) [129].

$$\eta = \frac{hN_{Av}}{V_m} exp\left(\frac{G^{*}}{RT}\right) \quad (16)$$

where h is Planck's constant, N_{Av} Avogadro's number, V_m the molar volume calculated from the previous density volume, R the gas constant, and G^{*} the molar activation energy for viscous flow:

$$G^{*} = \sum x_{quad}\left(A_{quad} + B_{quad}T\right) \quad (17)$$

where x_{quad} is the mole fraction of quadruplets, and A_{quad} and B_{quad} are adjustable parameters.

The quadruplets of the quasi-chemical model can be viewed as structural units, and the liquid as a lattice with empty sites (vacancies) and sites filled with the structural units [129]. When a structural unit acquires sufficient energy, or more specifically the activation energy G^{*}/N_{Av}, it can move from an occupied site to a vacancy. Because the viscosity of the melt is directly linked to its structure, it is also linked to the concentration of the structural units (the quadruplets). This approach has been followed to model the viscosity in the nuclear fuel systems LiF-ThF_4, LiF-UF_4, LiF-ThF_4-UF_4 and NaCl-UCl_3 [91]. It should be noted that the "traditional" quasi-chemical formalism was used, with fixed coordination numbers. In the work of Robelin and Chartrand on the NaF-AlF_3-CaF_2-Al_2O_3 system [129], the coupled thermodynamic-viscosity model also considered varying coordination numbers with the inclusion of Na^{+}, Al^{3+}_{V}, Al^{3+}_{IV}, Al^{6+}_{2}, Ca^{2+}, F^{-} and O^{2-}, respectively.

6. Conclusions and recommendations for further research

This review has given an overview of the current state of knowledge on the structural properties of actinide bearing chloride and fluoride melts, and their relationship to excess thermodynamic properties, density and viscosity. Generally, a strengthening of the local structure is observed upon melting of the pure actinide halides and their mixtures. A decrease in the coordination number in the first solvation shell around the actinide cation is moreover observed with increasing temperature, which is related to a decrease in density, increased thermal disorder and faster exchange rates of the halide anions in the solvation shell. Trends in mixtures with alkali metals have been discussed, including trends as a function of the alkali metal cation, actinide cation, temperature, composition for a single system, halide anion, and valence state of the actinide cation. Moving to the thermochemical properties, a decrease in thermodynamic stability along the series of the actinides trihalides and tetrahalides (from Th to Am) was noted, as exemplified by the evolution of the melting temperature and sublimation enthalpies, which is related to the effect of the 5*f* valence electrons on the bonding properties. The relationship between mixing enthalpy and local structure properties was then discussed: the position and value of the minima in the curves is related to the formation of isolated complexes, and to the transition from a molecular melt to one where oligomerization takes place. The relationship to other thermophysical properties (density/viscosity) was also illustrated. Finally, an overview of modelling methods of the thermodynamic, density and viscosity properties at the mesoscale based on the CALPHAD methodology was given. The quasi-chemical model in the quadruplet approximation is to this date the reference for the chloride and fluoride salts, with recent efforts to include variable coordination numbers, and to reproduce the chemical speciation as given by the output of molecular dynamic simulations. This approach leads to a better agreement with phase equilibrium data, and is expected to yield better predictive capabilities in regions of temperatures/compositions not accessible experimentally.

This overview has also allowed to identify gaps in knowledge, and to formulate recommendations for further research:

- the crystal structure of UF_3 (reported in the $P6_3cm$ space group) needs to be re-visited. It is suspected to belong to the $P\bar{3}c1$ symmetry like the rest of the series of actinide trifluorides;
- experimental investigations of the structural properties of the actinide halides are still scarce: only ThF_4, UF_4 and UCl_3 have been investigated in detail. Only one Raman study of $ThCl_4$ has been reported. EXAFS or neutron diffraction measurements would be extremely valuable. No experimental work has been performed to this date on molten UCl_4. No data seem to be available on molten UF_3, neither experimental nor computational;

- for the binary alkali metal-actinide halide mixtures: no data is available to this date on mixtures with UF_3. The local structures of chloride salts are generally less studied than the fluoride salts. There is a need for experimental data (EXAFS, ND, XRD) on $ThCl_4$ (only one Raman study), UCl_4 and UCl_3 based systems. There are also no data on Pu, Np or Am containing salts due to the even bigger challenges associated with those experiments (highly radioactive materials requiring multiple containments). This would be very useful however for salt systems with TRans-Uranic (TRU) mixtures including Pu, Np, Am and Cm, coming from the spent fuel of current Light Water Reactors [6];
- the ternary mixtures have been mostly investigated with computational methods: there is a need for experimental data to benchmark the results of the simulations;
- the knowledge acquired has been mostly for the base fuel salt. But data on actinide mixtures with key fission products (e.g. Cs, Ba, Se, Ce, Zr) and corrosion products (e.g. Cr) will also be required since the composition of the fuel evolves during irradiation;
- regarding the thermochemical properties: a re-assessment of the sublimation enthalpy of AmF_3 is necessary as it does not follow the trend of the rest of the actinide series;
- the mixing enthalpy data is challenging to collect but essential when it comes to modelling the thermodynamics of the salt systems by the CALPHAD method. Data on actinide containing systems are very scarce (limited to a few points in AF-ThF_4 (A = Li, Na, K), NaCl-UCl_3 and KCl-UCl_3. There is a real need for collection of such data on UF_4, UF_3, PuF_3, UCl_4, $ThCl_4$, and $PuCl_3$ containing systems.
- finally, the coupled structural-thermodynamic-density–viscosity modelling methodology based on the QCM in the quadruplet approximation needs to be tested and developed further on ternary, quaternary and higher order systems as the fuel becomes a multi-component system during the fission process. Such models are essential and a stringent requirement for the safety analysis of MSRs during normal operation and accidental conditions.

Declaration of Competing Interest

The authors declare that they have no known competing financial interests or personal relationships that could have appeared to influence the work reported in this paper.

Acknowledgements

The author thanks P. Souček and R.J.M. Konings from the JRC-Karlsruhe (Joint Research Centre, European Commission) for sharing their X-ray diffraction data on UF_3, NpF_3 and PuF_3.

References

[1] K. Sridharan, T.R. Allen, Molten Salts Chemistry: From Lab to Applications, Chapter 12: Corrosion in Molten Salts, Elsevier, 2013, pp. 241–267.
[2] T. Bauer, N. Pfleger, D. Laing, W.-D. Steinmann, M. Eck, S. Kaesche, Molten Salts Chemistry: From Lab to Applications, Chapter 20: High-Temperature Molten Salts for Solar Power Application, Elsevier, 2013, pp. 415–438.
[3] T. Ihli, T.K. Basu, L.M. Giancarli, S. Konishi, S. Malang, F. Najmabadi, S. Nishio, A.R. Raffray, C.V.S. Rao, A. Sagara, Y. Wu, Fusion Eng. Des. 83 (2008) 912–919.
[4] S. Delpech, C. Cabet, C. Slim, G.S. Picard, Mater. Today 13 (2010) 34–41.
[5] O. Beneš, R.J.M. Konings, Comprehensive Nuclear Materials, Chapter 5.18: Molten Salt Reactor Fuel and Coolant 5 (2020) 609–644.
[6] E. Capelli, Comprehensive Nuclear Materials, Chapter 7.07: Halides of the Actinides and Fission Products Relevant for Molten Salt Reactors 7 (2020) 256–283.
[7] A.E. Gheribi, D. Corradini, L. Dewan, P. Chartrand, C. Simon, P.A. Madden, M. Salanne, Mol. Phys. 112 (2014) 1305–1312.
[8] E.S. Bettis, R.W. Schroeder, G.A. Cristy, H.W. Savage, R.G. Affel, L.F. Hemphill, Nucl. Sci. Eng. 2 (1957) 804–825.
[9] P.N. Haubenreich, J.R. Engel, Nucl. Technol. 8 (1970) 118–136.
[10] S. Delpech, E. Merle-Lucotte, D. Heuer, M. Allibert, V. Ghetta, C. Le-Brun, X. Doligez, G. Picard, J. Fluorine Chem. 130 (2009) 11–17.
[11] A. Nuttin, D. Heuer, A. Billebaud, R. Brissot, C. Le Brun, E. Liatard, J.M. Loiseaux, L. Mathieu, O. Meplan, E. Merle-Lucotte, H. Nifenecker, F. Perdu, S. David, Prog. Nucl. Energ. 46 (2005) 77–99.
[12] A. Tosolin, P. Souček, O. Beneš, J.-F. Vigier, L. Luzzi, R.J.M. Konings, J. Nucl. Mater. 503 (2018) 171–177.
[13] O. Beneš, R.J.M. Konings, J. Nucl. Mater. 375 (2008) 202–208.
[14] Thermodynamic database on molten salt reactor systems , Joint Research Centre-Karlsruhe, European Commission.
[15] M. Salanne, C. Simon, P. Turq, R. Heaton, P. Madden, J. Phys. Chem. B 110 (2006) 11461–11467.
[16] M. Salanne, C. Simon, P. Turq, P. Madden, J. Phys. Chem. B 111 (2007) 4678–4684.
[17] M.-T. Nguyen, R. Rousseau, P.D. Paviet, V.-A. Glezakou, ACS Appl. Mater. Interfaces 13 (2021) 53398–53408.
[18] A.L. Smith, M.N. Verleg, J. Vlieland, D. de Haas, J.A. Ocádiz Flores, P. Martin, J. Rothe, K. Dardenne, M. Salanne, A.E. Gheribi, E. Capelli, L. van Eijck, R.J.M. Konings, J. Synchrotron Rad. 26 (2019) 124–136.
[19] O. Beneš, P. Souček, Advances in Nuclear Fuel Chemistry, Chapter 6: Molten salt reactor fuels, volume 5, 2020, 249-272
[20] A.L. Smith, E. Capelli, R.J.M. Konings, A.E. Gheribi, J. Mol. Liq. 299 (2020) 112165.
[21] J.A. Ocádiz Flores, A.E. Gheribi, J. Vlieland, D. de Haas, K. Dardenne, J. Rothe, R. J.M. Konings, A.L. Smith, Phys. Chem. Chem. Phys. 23 (2021) 11091–11103.
[22] A.-L. Rollet and M. Salanne. Annu. Rep. Prog. Chem., Sect. C 107 (2011) 88–123.
[23] C. Legein, O. Péron, B. Boulard, F. Fayon, C. Martineau, M. Body, J.Y. Buzaré, D. Massiot, E. Durand, A. Tressaud, A. Demourges, Inorg. Chem. 45 (2006) 10636–10641.
[24] R. Schmidt, B.G. Müller, Z. Anorg. Allg. Chem. 625 (1999) 605–608.
[25] R.D. Shannon, Acta Cryst. A 32 (1976) 751–767.
[26] J.T. Mason, M.C. Jha, P. Chiotti, J. Less-Common Met. 34 (1974) 143–151.
[27] J.A. Ocádiz Flores, B.A.S. Rooijakkers, R.J.M. Konings, A.L. Smith, Thermo 1 (2021) 122–133.
[28] M.P. Vorobei, A.E. Chernakov, O.V. Skiba, V.N. Desyatnik, Russ. J. Inorg. Chem. 16 (12) (1971) 1793–1794.
[29] P. Villars, K. Cenzual, ASM International, Materials Park, Ohio, USA, Technical report, (2020/2021).
[30] S.S. Rudel, H. Lars Deubner, B. Scheibe, M. Conrad, F. Kraus, Z. Anorg, Allg. Chem. 644 (2018) 323–329.
[31] P. Soucek, A.L. Smith, Private communication, refinement performed on data provided by the Joint Research Centre (European Commission) (JRC Karlsruhe), 2021.
[32] S.E. Nave, R.G. Haire, P.G. Huray, Phys. Rev. B 28 (1983) 2317–2327.
[33] S. Kern, D. Hoisington, G.H. Lander, J. Hayward, S. Roberts, J.W. Jr. Richardson, F.J. Rotella, L. Soderholm, B. Cort, M.C. Tinkle, M. West. J. Chem. Phys. 101 (1994) 9333–9337.
[34] L.B. Asprey, R.G. Haire, Inorg. Nucl. Chem. Lett. 9 (1973) 1121–1128.
[35] D. Brown, T.L. Hall, P.T. Moseley, J. Chem. Soc., Dalton Trans. (1973) 686–691.
[36] T. Schleid, G. Meyer, L.R. Morss, J. Less-Common Met. 132 (1987) 69–77.
[37] H. Hayashi, M. Takano, M. Kurata, K. Minato, J. Nucl. Mater. 440 (2013) 477–479.
[38] J.H. Burns, J.R. Peterson, J.N. Stevenson, J. Inorg. Nucl. Chem. 37 (1975) 743–749.
[39] T. Schleid, L.R. Morss, G. Meyer, J. Less-Common Met. 127 (1987) 183–187.
[40] M. Salanne, C. Simon, P. Turq, N. Ohtori, P.A. Madden, Molten Salts Chemistry, From Lab to Applications, Chapter 1: Modeling of Molten Salts, 2013.
[41] P.A. Madden, M. Salanne, Thorium Energy for the World: Proceedings of the ThEC13 Conference, CERN, Globe of Science and Innovation, Springer, Geneva, Switzerland, 2016, pp. 111–116.
[42] J. Dai, D. Long, P. Huai, Q. Li, J. Mol. Liq. 211 (2015) 747–753.
[43] G.M. Photiadis, G.N. Papatheodorou, J. Chem. Soc., Dalton Trans. (1999) 3541–3548.
[44] B. Li, S. Dai, D.-E. Jiang, ACS Appl. Energy Mater. 2 (2019) 2122–2128.
[45] Y. Okamoto, F. Kobayashi, T. Ogawa, J. Alloys Compd. 271–273 (1998) 355–358.
[46] G.W. Neilson, A.K. Adya, S. Ansell, Annu. Rep. Prog. Chem., Sect. C: Phys. Chem. 98 (2002) 273–322.
[47] A.K. Adya, H. Matsuura, R. Takagi, L. Rycerz, M. Gaune-Escard, Proc. 341–355 (1999) 41.
[48] Y. Okamoto, P.A. Madden, K. Minato, J. Nucl. Mater. 344 (2005) 109–114.
[49] G.I.L. van Oudenaren, J.A. Ocádiz-Flores, A.L. Smith, J. Mol. Liq. 342 (2021) 117470.
[50] A.L. Ankudinov, B. Ravel, J.J. Rehr, S.D. Conradson, Phys. Rev. B: Condens. Matter Mater. Phys. 58 (1998) 7565–7576.
[51] C. Pauvert, M. Salanne, D. Zanghi, C. Simon, S. Reguer, D. Thiaudière, Y. Okamoto, H. Matsuura, C. Bessada, J. Phys. Chem. B 115 (2011) 9160–9167.
[52] C. Bessada, D. Zanghi, O. Pauvert, L. Maksoud, A. Gil-Martin, V. Sarou-Kanian, P. Melin, S. Brassamin, A. Nezu, H. Matsuura, J. Nucl. Mater. 494 (2017) 192–199.
[53] J.-B. Liu, X. Chen, Y.-H. Qiu, C.-F. Xu, W.H. Eugen Schwarz, J. Li, J. Phys. Chem. B 118 (2014) 13954–13962.
[54] D. Alders, J.A. Ocádiz Flores, C. Vriends, M. van den Berg, and A.L. Smith. in preparation (2022).

[55] J.-B. Liu, X. Chen, J.-B. Lu, H.-Q. Cui, J. Li, J. Comput. Chem. 39 (2018) 2432–2438.
[56] T. Dumaire, J.A. Ocádiz-Flores, R.J.M. Konings, A.L. Smith. CALPHAD, submitted, 2022.
[57] C. Bessada, D. Zanghi, M. Salanne, A. Gil-Martin, M. Gibilaro, P. Chamelot, L. Massot, A. Nezu, H. Matsuura, J. Mol. Liq. 307 (2020) 112927.
[58] X. Guo, H. Qian, J. Dai, W. Liu, J. Hu, R. Shen, J. Wang, J. Mol. Liq. 277 (2019) 409–417.
[59] L.C. Dewan, C. Simon, P.A. Madden, L.W. Hobbs, M. Salanne, J. Nucl. Mater. 434 (2013) 322–327.
[60] J.A. Ocádiz Flores, A.E. Gheribi, J. Vlieland, K. Dardenne, J. Rothe, R.J.M. Konings, A.L. Smith, J. Mol. Liq. 331 (2021) 115820.
[61] B. Li, S. Dai, D. Jiang, ChemPhysChem (2022).
[62] B. Li, S. Dai, D.-E. Jiang, J. Mol. Liq. 299 (2020) 112184.
[63] O. Abbenhuis, J.A. Ocadiz Flores, A.L. Smith, unpublished data, 2022.
[64] Y. Okamoto, T. Yaita, H. Shiwaku, S. Suzuki, P.A. Madden, Recent status of XAFS work on molten salt systems in Spring-8. The 4th workshop on speciation techniques and facilities for radioactive materials at synchrotron light sources, 35-44, OECD Publications, Paris, France, 2006.
[65] X. Li, J. Song, S. Shi, L. Yan, Z. Zhang, T. Jiang, S. Peng, J. Phys. Chem. A 121 (2017) 571–578.
[66] J. Song, S. Shi, X. Li, L. Yan, J. Mol. Liq. 234 (2017) 279–286.
[67] J.-X. Dai, W. Zhang, C.-L. Ren, H. Han, X.-J. Guo, Q.-N. Li, J. Nucl. Mater. 511 (2018) 75–82.
[68] X. Li, N. Li, W. Liu, Z. Tang, J. Wang. Sol. Energ. Mat. Sol. C. 210 (2020) 110504.
[69] C.-H. Huang, M.H. Brooker, Chem. Phys. Lett. 43 (1976) 180–182.
[70] K. Balasubrahmanyam, J. Chem. Phys. 44 (1966) 3270–3273.
[71] S. Biggin, M. Gay, J.E. Enderby, J. Phys. C Solid State Phys. 17 (1984) 977–985.
[72] L. Pusztai, R.L. McGreevy, J. Phys-Condens. Mat. 13 (2001) 7213–7222.
[73] W. Liang, J. Wu, H. Ni, G. Lu, J. Yu, J. Mol. Liq. 298 (2020) 112063.
[74] T. Xu, X. Li, L. Guo, F. Wang, Z. Tang, Sol. Energy 209 (2020) 568–575.
[75] W. Liang, G. Lu, J. Yu, J. Mol. Liq. 309 (2020) 113131.
[76] R.J.M. Konings, O. Benes, A. Kovács, D. Manara, D. Sedmidubský, L. Gorokhov, V.S. Iorish, V. Yungman, E. Shenyavskaya, and E. Osina. J. Phys. Chem. Ref. Data 43 (2014) 013101.
[77] A. Tosolin, E. Capelli, R.J.M. Konings, L. Luzzi, O. Beneš, J. Chem. Eng. Data 64 (2019) 3945–3950.
[78] R.J.M. Konings, J.P.M. van der Meer, E. Walle, Chemical Aspects of Molten Salt Reactor Fuel and Coolant, European Commission, JRC, Institute for Transuranium Elements, Karlsruhe, Germany, Technical report, 2005.
[79] M. Beilmann, O. Beneš, R.J.M. Konings, Th. Fanghänel, J. Chem. Thermodyn. 57 (2013) 22–31.
[80] V. Danek, Physico-Chemical Analysis of Molten Electrolytes, Elsevier, 2006.
[81] M. Gaune-Escard, Molten Salts: From Fundamentals to Applications, Springer Science + Business Media Dordrecht, 2002.
[82] E. Capelli, O. Beneš, M. Beilmann, R.J.M. Konings, J. Chem. Thermodyn. 58 (2013) 110–116.
[83] G.N. Papatheodorou, T. Ostvold, J. Phys. Chem. 78 (1974) 181–185.
[84] L. Rycerz, J. Kapala, M. Gaune-Escard, J. Mol. Liq. 342 (2021) 116963.
[85] H. Matsuura, R. Takagi, L. Rycerz, M. Gaune-Escard, J. Nucl. Sci. Technol. 3 (2002) 632–634.
[86] M. Blander, J. Alloy. Compd. 321 (2001) 164–168.
[87] O.J. Kleppa, F.G. McCarty, J. Chem. Phys. 70 (1966) 1249–1255.
[88] G. Hattem, F. Tabaries, M. Gaune-Escard, Thermochim. Acta 149 (1989) 15–26.
[89] M.B.J.W. Schreuder, J.A. Ocádiz Flores, A.E. Gheribi, O. Beneš, J.-C. Griveau, E. Colineau, R.J.M. Konings, A.L. Smith, J. Phys. Chem. B 125 (2021) 8558–8571.
[90] J.A. Ocádiz-Flores, E. Carré, J.-C. Griveau, E. Colineau, E. Capelli, P. Souček, O. Beneš, R.J.M. Konings, A.L. Smith, J. Chem. Thermodyn. 145 (2020) 106069.
[91] J.A. Ocádiz Flores, R.J.M. Konings, A.L. Smith, J. Nucl. Mater., 561, 2022, 153536
[92] M. Gaune-Escard, A. Bogacz, L. Rycerz, W. Szczepaniak, Thermochim. Acta 236 (1994) 67–80.
[93] K.C. Hong, O.J. Kleppa, J. Phys. Chem. 83 (1979) 2589–2593.
[94] F. Abdoun, M. Gaune-Escard, G. Hattem, J. Phase Equilib. 18 (1997) 6–20.
[95] M. Gaune-Escard, L. Rycerz, M. Hoch, J. Mol. Liq. 83 (1999) 83–94.
[96] J.L. Holm, O.J. Kleppa, Inorg. Chem. 8 (1968) 207–212.
[97] G.N. Papatheodorou, O.J. Kleppa, J. Chem. Phys. 47 (1967) 2014–2020.
[98] H. Reiss, J.L. Katz, O.J. Kleppa, J. Chem. Phys. 36 (1962) 144–148.
[99] H.T. Davis, S.A. Rice, J. Chem. Phys. 41 (1) (1964) 14–24.
[100] H.T. Davis, J. Chem. Phys. 41 (9) (1964) 2761–2766.
[101] H.T. Davis, J. Phys. Chem. 76 (11) (1972) 1629–1631.
[102] S.N. Flengas, A.S. Kucharski, Can. J. Chem. 49 (1971) 3971–3985.
[103] J. Schorne-Pinto, J.A. Yingling, M.S. Christian, A.M. Mofrad, M.A.A. Aslani, T.M. Besmann, ACS Omega 7 (2022) 362–371.
[104] K.C. Hong, O.J. Kleppa, J. Phys. Chem. B 82 (1978) 1596–1603.
[105] V.N. Desyatnik, S.F. Katyshev, S.P. Raspopin, Y.F. Chervinskii, Sov. Atom. Energy 39 (1975) 649–651.
[106] Y.F. Chervinskii, V.N. Desyatnik, A.I. Nechaev, Zh. Fiz. Khim. 56 (1982) 1946–1949.
[107] V.N. Desyatnik, A.A. Klimenkov, N.N. Kurbatov, A.I. Nechaev, S.P. Raspopin, Yu.F. Chervinskii, Sov. Atom. Energy 51 (1981) 807–810.
[108] V.N. Desyatnik, A.I. Nechaev, Yu.F. Chervinskii, Sov. Atom. Energy 46 (1979) 354–355.
[109] V.N. Desyatnik, A.I. Nechaev, Y.F. Chervinskii, Zh. Prikl. Khim. 54 (1981) 2310–2313.
[110] H.L. Lukas, S.G. Fries, B. Sundman, Computational Thermodynamics, Cambridge University Press, The Calphad Method, 2007.
[111] B. Sundman, Q. Chen, Y. Du, J. Phase Equilib. Diffus 39 (2018) 678–693.
[112] A.D. Pelton, S.A. Degterov, G. Eriksson, C. Robelin, Y. Dessureault, Metall. Mater. Trans. B 31 (2000) 651–659.
[113] A.D. Pelton, P. Chartrand, Metall. Mater. Trans. A 32 (2001) 1355–1360.
[114] P. Chartrand, A.D. Pelton, Metall. Mater. Trans. A 32 (2001) 1397–1407.
[115] A.D. Pelton, P. Chartrand, G. Eriksson, Metall. Mater. Trans. A 32 (2001) 1409–1416.
[116] H. Yin, P. Zhang, X. An, J. Cheng, X. Li, S. Wu, X. Wu, W. Liu, L. Xie, J. Fluorine Chem. 209 (2018) 6–13.
[117] S. Wu, X. Li, P. Zhang, X. An, and L. Xie. Chem. Res. Chin. Univ. (2018).
[118] A.D. Pelton, Phase Diagrams and Thermodynamic Modeling of Solutions, Chap 16: Single-Lattice Models With Short Range Ordering (SRO), Elsevier, Amsterdam, The Netherlands, 2019, pp. 253–294.
[119] T.M. Besmann, J. Schorne-Pinto, Thermo 1 (2021) 168–178.
[120] E.A. Guggenheim, Mixtures, Clarendon Press, Oxford, UK, 1952.
[121] A.D. Pelton, M. Blander, Metall. Trans. B-Process, Metall. 17 (1986) 805–815.
[122] C. Robelin, P. Chartrand, Metall. Mater. Trans. B 38 (2007) 881–892.
[123] C. Robelin, P. Chartrand, J. Chem. Thermodyn. 57 (2013) 387–403.
[124] O. Benš, R.J.M. Konings, J. Chem. Thermodyn. 41 (2009) 1086–1095.
[125] C. Robelin, P. Chartrand, G. Eriksson, Metall. Mater. Trans. B 38 (2007) 869–879.
[126] S. Glasstone, K.J. Laidler, H. Eyring, The Theory of Rate Processes - The Kinetics of Chemical Reactions, Viscosity, Diffusion and Electrochemical Phenomena, McGraw-Hill Book Company Inc., New York & London, 1941.
[127] H. Eyring, D. Henderson, B.J. Stover, E.M. Eyring, Statistical Mechanics and Dynamics. (1964).
[128] H. Eyring, D. Henderson, and T. Ree. Thermodynamic and Transport Properties of Liquids. Progr. Intern. Res. Thermodyn. Transport Properties Papers, Symp. Thermophys. Properties. Princeton, New Jersey, 1962, second edition, (1962).
[129] C. Robelin, P. Chartrand, J. Chem. Thermodyn. 43 (2011) 764–774.
[130] J. C. Ard, J. A. Yingling, K. E. Johnson, J. Schorne-Pinto, M. Aziziha, C. M. Dixon, M. S. Christian, J. W. McMurray and T. M. Besmann, "Development of the Molten Salt Thermal Properties Database – Thermochemical (MSTDB–TC), example applications, and LiCl–RbCl and UF3–UF4 system assessments", J. Nucl. Mater., 563 (2022) 153631.